Impact of the competition between aggregation and surface growth on the morphology of soot particles formed in an ethylene laminar premixed flame

José Morán, Alexandre Poux, Jérôme Yon

Impact of the competition between aggregation and surface growth on the morphology of soot particles formed in an ethylene laminar premixed flame

José Morán[a], Alexandre Poux[a], Jérôme Yon[a,*]

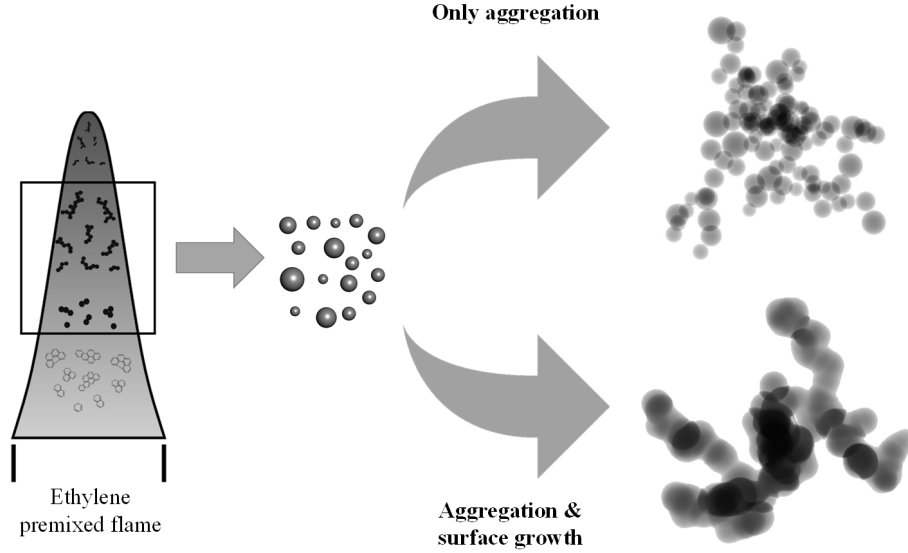[a]*Normandie Univ, UNIROUEN, INSA Rouen, CNRS, CORIA, 76000 Rouen, France*

Abstract

Soot particle surface growth may have a significant impact on aggregation kinetics, particle morphology, and both aggregate and monomer size distributions. Particularly, the morphological effects of surface growth are currently poorly understood. This is complex since surface growth also affects the kinetics of aggregation resulting in a time-dependent competition between both phenomena, producing very different morphological markers. The present study aims at improving our understanding of the morphological impact of surface growth by implementing this effect in a Monte Carlo discrete element code for the simulation of soot formation in an ethylene premixed flame. An asymptotic average primary particle overlapping $\sim 30\%$ is observed for different flame conditions. The primary particle coordination number is highly sensitive to surface growth rate and particle volume fraction, and maximum values are on average within the 4 - 8 range. The particle local compacity, as quantified by the packing factor, is also considerably increased when aggregates experience surface growth, contrarily to the fractal structure of individual aggregates that seems more dependent on the aggregation regime. Finally, surface growth narrows both the primary particle and aggregate size distributions.

Keywords: Soot, Aggregation, Surface Growth, Coordination Number, Overlapping

*Corresponding author.
E-mail address:* yon@coria.fr

Graphical abstract

1. Introduction

To understand the specific morphology of soot particles pollutants released to the atmosphere, it is prior necessary to understand how they are formed and how they evolve within flames. Up to now, most of the numerical studies have considered the role played by pure aggregation, explaining the fractal-like nature of these particles (Mountain et al. (1986); Isella & Drossinos (2010); Camejo et al. (2014); Inci et al. (2017); Morán et al. (2020b)). In this context, a recent study revealed that the change in regimes of both particle-particle interaction and also particle-gas interaction during the formation process has a significant impact on the particle size distribution, agglomeration kinetics, and particle morphology (Morán et al. (2020b)). However, limiting the study to the agglomeration alone (without considering additional mechanisms of soot formation) results in point-touching primary particles which are commonly not representative of experimentally measured particles. Notably, for particles formed in flames (such as soot), surface reactions and particularly surface growth cannot be neglected. This because they occur simultaneously with aggregation process producing overlapped primary particles (Oh & Sorensen (1997); Brasil et al. (1999)), as commonly observed in transmission electron microscopy (TEM) images of aged soot particles in diffusion and premixed flames (Wentzel et al. (2003); Cortés et al. (2018); Bourrous et al. (2018); Altenhoff et al. (2020)). This overlap is suspected to affect the particle surface area to volume ratio (specific surface area) which has been suggested as one of the most important dose metrics for nanoparticle toxicity by inflammatory response and oxidative stress of pulmonary cells (Stoeger et al. (2007); Hussain et al. (2009); Sager & Castranova (2009);

2

Gatoo et al. (2014); Schmid & Stoeger (2016); Kwon et al. (2020)). Surface growth may provide nearly all the mass of the ultimately formed soot particles in flames (Harris (1984); Harris & Weiner (1985)), in consequence, many authors attribute the primary particle overlapping to surface growth (Mitchell & Frenklach (2003); Balthasar & Frenklach (2005a); Morgan et al. (2007)). Nevertheless, some authors attribute monomer overlapping to partial sintering (Lapuerta et al. (2015); Ono et al. (2017)), or both partial sintering and surface growth (Hou et al. (2020)).

In addition to the impact of inter-penetrated primary particles on the specific surface area, it should be noted that primary particle overlapping plays an important role in soot particles radiative properties (Yon et al. (2015a); Doner et al. (2017); Sutcu et al. (2020)). Thus, it can also affect climate models and particle sizing by optical techniques such as time-resolved laser-induced incandescence. Indeed, the latter technique requires an accurate determination of both aggregate's volume and surface area (Bambha & Michelsen (2015); Liu et al. (2006); Patiño et al. (2020)). But also the amount of overlapping between monomers which influences the heat transfer (notably, conduction) rates with the surrounding gas (Johnsson et al. (2013)).

Surface growth is a complex chemical process involving the heterogeneous reaction between molecules and particles with time-evolving composition and consequently reactivity (Appel et al. (2000); Veshkini et al. (2014); Chen et al. (2015)). In this context, primary particle overlapping produced by surface growth has been shown by a few remarkable works (Mitchell & Frenklach (2003); Balthasar & Frenklach (2005a); Morgan et al. (2007); Kelesidis et al. (2017); Hou et al. (2020)) however, it has not been quantified and systematically studied. In the present work, we support the idea that a temporal competition between aggregation and surface growth mechanisms can affect the resulting particle morphology, and thus the degree of primary particle overlapping. This can be easily illustrated by considering two asymptotic cases. Let us firstly consider surface growth acting on isolated monomers is achieved before any aggregation takes place. This will naturally produce agglomerates made of point-touching large spheres (without overlapping), corresponding to the agglomerates formed under no surface growth (Mountain et al. (1986); Isella & Drossinos (2010); Camejo et al. (2014); Inci et al. (2017); Morán et al. (2020b)). Let us secondly consider that highly mobile initially isolated monomers collide and aggregate very quickly before any surface growth takes place. For sufficiently long subsequent residence time under surface growth, this will certainly produce nearly spherical very compact aggregates (Mitchell & Frenklach (1998, 2003); Balthasar & Frenklach (2005b)). In this context, the balance between aggregation and surface growth is suspected to play an important role in particle morphology. This balance is not trivial since both mechanisms are inter-dependent. Indeed, since surface growth increases the mass of individual clusters, it may also influence the kinetics of aggregation. The present work aims at studying this competition between aggregation and surface growth and its impact on particle morphology. To focus on these two mechanisms, we consider experimental data available for soot surface growth from a premixed laminar flame without considering the nucleation and particle fragmentation

3

induced by oxidation.

However, primary particle overlapping is not the only consequence of the simultaneous aggregation and surface growth. A special attention is paid to the particle coordination number n_c (i.e. the number of intersections of monomers with neighbors Weber & Friedlander (1997); Brasil et al. (2001)). Unfortunately, this parameter is commonly overlooked in the literature. And yet, along with the overlapping coefficient, it plays an important role in the fundamental physicochemical properties of aggregates such as the heat/electrical conduction, catalytic/chemical performance, radiative properties, and mechanical resistance (Rumpf (1958); Zahaf et al. (2015); Deng et al. (2016); Gensch & Weber (2017); Post et al. (2018)). The combination of the time-evolving overlapping and coordination number of primary particles makes the determination of aggregate volume and surface area quite challenging. Some numerical methods exist, such as the highly accurate libraries ARVO (Buša et al. (2005)) and SBL (Cazals et al. (2011)) as used in (Lazzari & Lattuada (2017); Eggersdorfer et al. (2012)), approximative ones by calculating the spherical caps (Brasil et al. (1999); Wentzel et al. (2003); Morán et al. (2018)) as done in (Morán et al. (2018); Lindberg et al. (2019a)), by using Monte Carlo methods (Mitchell & Frenklach (1998); Balthasar & Frenklach (2005b)), and based on aggregate discretization (Oh & Sorensen (1997); Schmid et al. (2006); Al Zaitone et al. (2009)). The aforementioned methods are commonly computationally expensive, especially the aggregate discretization and the accurate libraries ARVO or SBL. One exception is the approximative methods based on the spherical caps, however as further discussed later, they quickly fail when increasing primary particles overlapping and coordination number since multi-sphere intersections is neglected. In this context, we propose a new accurate semi-analytical and quite computationally cheap method to calculate both the aggregate's volume and surface area.

An additional fundamental question that arises when considering the complex morphological evolution of soot particles under surface growth is about the change in its fractal-like structure. Some authors have suggested that only the fractal prefactor should increase due to primary particle overlapping (Oh & Sorensen (1997); Brasil et al. (1999); Lapuerta et al. (2015)) at least for overlapping coefficients no larger than 30%. However, strong surface growth rates may lead to sphere-like particles that can hardly retain the same fractal structure (Mitchell & Frenklach (1998, 2003); Balthasar & Frenklach (2005b)). Most of the cited works are based on the population fractal structure derived from the fractal-law. However, remarkably different results are obtained when analyzing the morphology of individual aggregates as experimentally done by the box-counting method in Refs. (Wozniak et al. (2012); Altenhoff et al. (2020)), and recently numerically by analyzing the volume-based pair correlation function Yon et al. (2020). The latter enables accurate characterization of the aggregate morphology by determining the individual fractal dimension and packing factor (Heinson et al. (2012)). These parameters represent the global structure and the local compacity of aggregates, respectively. For this reason, this method is adopted in the present work to investigate the effect of surface growth on soot aggregates morphology.

2. Methodology

2.1. Surface growth model

As schematically shown in Fig. 1 and without loss of generality, an individual monomer belonging to an
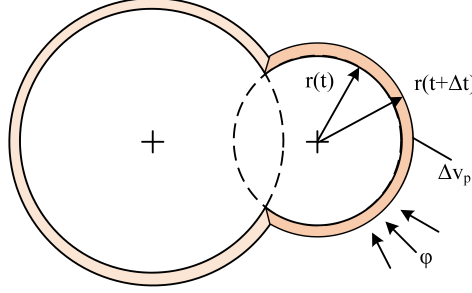

Figure 1: A molecular mass flow is making a dimer to increase in mass by surface reactions.

aggregate is increasing in radius from $r_p(t)$ to $r_p(t + \Delta t)$ due to a local adsorption governed by a specific surface mass flux density φ in $(kg/m^2/s)$ units during a time step Δt. In this context, the increase in the monomer mass and volume can be calculated as,

$$\Delta m_p = \Delta v_p \rho_p = \int_{s_p} \varphi ds_p \Delta t \tag{1}$$

where Δm_p and Δv_p represent respectively the increase in mass and volume and s_p is the surface area of the monomer exposed to the molecular flux φ. The ratio $\varphi/\rho_p = u$ is homogeneous to a velocity and can be interpreted as the surface growth rate. In addition, for small Δt and φ uniform along the primary sphere exposed surface area, Δv_p can be approximated as $\Delta v_p = s_p \Delta r$. Finally, combining this expression with Eq. (1) the following expression is obtained,

$$r_p(t + \Delta t) = r_p(t) + u\Delta t \tag{2}$$

Thus, under the assumption of uniform mass flux, it appears that the absolute increase in primary particle radius is uniform for all monomers belonging to an aggregate. Note that a similar approach has been carried out by Mitchell & Frenklach (1998). In this approach, the surface growth rate is a function of time because soot particles reactivity reduces when ageing through the flame (Frenklach & Wang (1991); Frenklach (1996); Veshkini et al. (2014); Chen et al. (2015); Russo et al. (2015)).

2.2. Numerical simulation of the coupled aggregation and surface growth

In the present study, the Monte Carlo Aggregation Code (MCAC, Morán et al. (2020a,b)) is used. It is adapted for taking the particle surface growth into account. In order to accurately simulate the particle dynamics and collisions with other clusters, the mass and friction coefficient has to be calculated by MCAC.

In the context of the present study, these two quantities have to be evaluated by considering the structure of aggregates under surface growth. The friction coefficient is calculated based on the method proposed by Yon et al. (2015b) who proposed the cluster friction coefficient f_{agg} to be proportional to the individual monomer friction one f_p according to the following power-law: $f_{agg} = f_p \left(N_{\mathrm{p,eff}}\right)^{\Gamma/D_f}$. Here, f_p is related to the average volume-equivalent primary particle diameter (Morán et al. (2020a)) and Γ is an empirical function depending on the monomer flow regime and D_f is the aggregate fractal dimension. Additionally, $N_{\mathrm{p,eff}}$ is the effective number of primary particles defined as $N_{\mathrm{p,eff}} = v/v_p$ where v and v_p are the aggregate and averaged primary particle volumes, respectively. Without overlapping between monomers we have: $N_{\mathrm{p,eff}} = N_{\mathrm{p}}$, with N_{p} the number of constituent primary particles in the aggregate. However, in the case of aggregates consisting of overlapped monomers, $N_{\mathrm{p,eff}}$ is smaller than N_{p}. For example, if two primary particles are perfectly overlapped we have $N_{\mathrm{p}} = 2$ but $N_{\mathrm{p,eff}} = 1$.

Thus, in order to evaluate $N_{\mathrm{p,eff}}$, the actual aggregate's volume must be determined. Without overlapping, we simply find $v = N_{\mathrm{p}} \times v_p$, which was used in our previous work (Morán et al. (2020b)). However, when primary particles are overlapped, we have to consider a correction factor $\alpha_v \in]0, 1]$ such that the total volume of the aggregate is $v = \alpha_v \times N_{\mathrm{p}} \times v_p$. Consequently the effective number of monomers is calculated as $N_{\mathrm{p,eff}} = \alpha_v N_{\mathrm{p}}$. For the aforementioned example of a totally overlapped dimer, $\alpha_v = N_{\mathrm{p,eff}}/N_{\mathrm{p}} = 1/2$. The same correction is naturally used for the evaluation of the particle mass $m = \rho_p \times \alpha_v \times N_{\mathrm{p}} \times v_p$. This correction is thoroughly explained in the following section.

2.3. Proposed volume and surface area approximation

In this section we propose two corrective factors $\alpha_v \in]0, 1]$ and $\alpha_s \in]0, 1]$ to calculate the volume and surface area of aggregates experiencing surface growth and therefore a certain overlap between the constituting primary particles. These factors are defined as a correction to bring to the volume and surface area evaluated without considering any overlapping, i.e. $v = \left(\sum_{i=1}^{N_p} \frac{4\pi}{3} r_{p,i}^3\right) \times \alpha_v$ and $s = \left(\sum_{i=1}^{N_p} 4\pi r_{p,i}^2\right) \times \alpha_s$. When particles do not experience surface growth then $\alpha_v = \alpha_s = 1$ and therefore the volume and surface area of aggregates correspond to the sum of the total spherical primary particle ones, respectively. When more than 2 primary particles are overlapped there is no analytical solution for α_v and α_s and only approximative expressions can be obtained only when neglecting multi-sphere intersection (Brasil et al. (1999); Wentzel et al. (2003); Morán et al. (2018); Lindberg et al. (2019b)). Indeed, neglecting this term is commonly done in the literature (Brasil et al. (1999); Morán et al. (2018); Lindberg et al. (2019a)) however it can lead to a large underestimation of the real particle's volume and surface area. This simplification can also produce negative values in certain cases of high overlapping and multi-sphere intersection. Here a method to estimate the volume and surface area of fractal-like aggregates composed of N_p primary particles is introduced by proposing an analytical correction for the multi-sphere intersection. The derivation of the proposed volume

and surface area factors is provided in Appendix A, and the final expressions are given as follows,

$$\alpha_v = 1 - \frac{1}{4}\overline{n_c}\left(3c_{20}^2 - c_{30}^3\right) + \beta_v \tag{3a}$$

$$\alpha_s = 1 - \frac{1}{2}\overline{n_c}c_{10} + \beta_s \tag{3b}$$

where $\overline{n_c}$ is the average coordination number over the primary particles of a given aggregate (Kauffman (2013)), c_{q0} is the q-moment average overlapping coefficient. These parameters are calculated based on all the intersections between monomers belonging to an aggregate. Additionally, β_v and β_s are the proposed correction factors for multi-sphere intersection:

$$\beta_v = a_v c_{30}^3(\overline{n_c} - \overline{n_{c,\min}}) + b_v(\overline{n_c} - \overline{n_{c,\min}})^{1.5} \tag{4a}$$

$$\beta_s = a_s c_{10}^2(\overline{n_c} - \overline{n_{c,\min}}) + b_s(\overline{n_c} - \overline{n_{c,\min}})^2 \tag{4b}$$

where $\overline{n_{c,\min}} = 2(N_p - 1)/N_p$ is the minimum average coordination number. It ensures $\beta_v = \beta_s = 0$ when no multi-sphere intersection exists, i.e. when $\overline{n_c} = \overline{n_{c,\min}}$. For example, for a dimer $\overline{n_c} = \overline{n_{c,\min}} = 1$ can be easily verified. This is true for any agglomerate consisting of point-touching primary particles. In the limit $N_p \longrightarrow \infty$ this expression leads to $\overline{n_{c,\min}} \longrightarrow 2$, this is quite robust regarding particles morphology considering that both DLCA and RLCA agglomerates show $\overline{n_{c,\min}} \longrightarrow 2$ for very large agglomerates (Lattuada et al. (2003)). This parameter is also unaffected by the primary particle polydispersity for DLCA agglomerates (Yon et al. (2020)). The same conclusion has been obtained for monomer-cluster aggregation mechanisms where much compact structures are formed (Brasil et al. (2001)), and also for cluster-cluster tunable aggregates (Melas et al. (2014)). In these expressions a_v, b_v, a_s, and b_s are constant values obtained by post-processing fits (see Appendix A). Considering primary particles as monodisperse is a good conceptual starting point however, soot primary particles are never monodisperse (Cortés et al. (2018); Patiño et al. (2020)) and therefore an equivalent expression is provided in this Appendix for polydisperse monomers.

3. Numerical simulations

The Monte Carlo Aggregation Code (MCAC) introduced and validated in the previous works (Morán et al. (2020a,b)) is adapted here to simulate soot particles aggregation and surface growth by considering the correction factor α_v in the evaluation of the particle mass and friction coefficient as discussed in the previous sections. The simulations are conducted by fixing $T = 1700$ K and $p = 1$ atm, corresponding to the ethylene laminar premixed flames studied by Harris (1984, 1990). More recent measurements have confirmed the temperature to be within the $1650 - 1770$ K range (Sirignano et al. (2017)), and for a wider range of argon-ethylene premixed flames between 1600 and 1900 K by Abid et al. (2008).

As shown in Fig. 2, two scenarios of time-decreasing surface growth rate u are considered in the present study. These rates are based on the referred experimental measurements considering a constant soot particle mass bulk density $\rho_p = 1800$ kg/m^3 for two flame conditions. This corresponds to soot particles with low organic content Ouf et al. (2019a). To ease the interpretation of results they are referred all along the manuscript based on their initial surface growth rate ($u_0 = 0, 0.4$, and 0.6 (see Fig. 2)) and particle volume fraction f_v. Cases with $u_0 = 0.4$ and $u_0 = 0.6$ correspond to C/O = 0.82, and 0.94 rich premixed flames, respectively. This was achieved by changing the fuel-oxidizer equivalence ratio (Harris (1984, 1990)). As a reference case, we also consider a simulation of pure aggregation ($u = 0$).
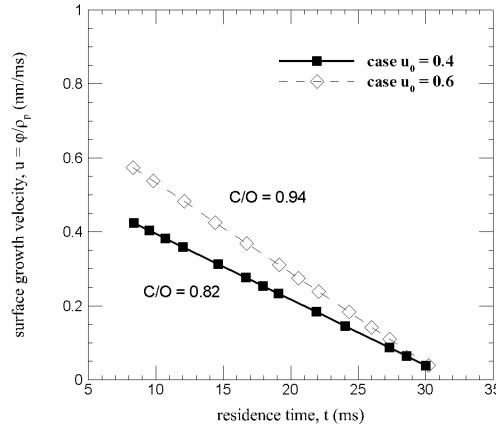

Figure 2: The surface growth rates considered in the present work (Harris (1990)).

Based on the available data of surface growth rates from Harris (1984), the current modeling covers the $8.3 - 30$ ms range in residence time, corresponding approximately to $5 - 25$ mm in height above the burner. According to the referred measurements, the initial geometric mean diameter is $d_p = 8$ nm. Simulating aggregation for shorter residence times is challenging without considering nucleation and nascent soot coalescence. Then, starting the siumulation at $d_p = 8$ nm consists in considering mature soot without nucleation, sintering and coalescence (D'Anna et al. (2010); Salenbauch et al. (2018)). We hypothesize that aggregation is negligible at residence times $t \leq 8.3$ ms due to particle coalescence. The primary particle geometric standard deviation is fixed to $\sigma_{p,geo} = 1.2$ at the beginning of the simulation in accordance with data from the literature of premixed flames (Betrancourt et al. (2017); Altenhoff et al. (2020); Hou et al. (2020)).

Based on (Harris (1984, 1990)), an initial particle volume fraction of $f_v = 0.118$ ppm is considered for cases with $u = 0$, $u_0 = 0.4$ and $u_0 = 0.6$. In addition to the change of surface growth rate, we also evaluate the impact of the initial volume fraction. To this end, we also simulate the case $u_0 = 0.6$ by considering a larger volume fraction, namely $f_v = 0.357$ ppm. In consequence, a total of four cases are simulated in the

present work, corresponding to different levels of surface growth and initial volume fraction. In addition, for each simulation, a total of 1024 primary particles are randomly distributed in a cubic box avoiding overlap between each other (Morán et al. (2020a)). This number is smaller than in our previous work (Morán et al. (2020b)) since surface growth considerably increases the CPU time cost of simulations. Indeed, one typical simulation of this work takes between 15 to 19 h in CPU time (Intel Xeon E5-2683 v4, with 20 Gb of RAM memory). A total of 10 simulations are carried out for each case and results presented later correspond to the average over these simulations. Finally, the current procedure is validated by comparison of the kinetics of aggregation and aggregate size distribution for the case $u = 0$ with macroscopic Population Balance simulations. In this context, the nodal method proposed by Prakash et al. (2003) for coalescing spheres is adapted to aggregation based on the method proposed by Thajudeen et al. (2012) and the results are reported in pages 2 - 4 of the Supporting Material. Considering the uncertainties of Population Balance simulations (particularly in terms of aggregate's fractal dimension and prefactor), the comparison reports satisfactory consistent results.

4. Results and discussions

4.1. Aggregation and flow regimes

Smaller soot particles tend to agglomerate more ballistically while larger particles or aggregates come to contact in diffusive motion. At the same time, the interaction with the surrounding gas transit from free-molecular to near continuum. This simultaneous change in aggregation and flow regime can have a siginificant impact on aggregation kinetics, particle morphology, and the particle size distribution Morán et al. (2020b). Fig. 3a presents the evolution of the aggregation (nearest-neighbor Knudsen number Kn_n; ratio between the persistence distance and nearest-neighbor distance) and fluid flow regimes (gas Knudsen number Kn_g; ratio between the gas mean free path and particle mobility radius). This type of representation has been originally suggested by Thajudeen et al. (2015) adopted, and modified by Morán et al. (2020b). Due to the flame temperature, particle size and volume fraction, a simultaneous transition in aggregation (from near-ballistic to diffusive) and flow regime (from free molecular to near continuum) is observed. While cases $u_0 = 0.4$ and $u_0 = 0.6$ (low f_v) show a similar evolution, case $u_0 = 0.6$ (high f_v) is much ballistic at the beginning and much diffusive at the end of the simulation. In all cases, near-ballistic Limited Cluster Aggregation (BLCA) under free molecular flow regime is only observed at the very beginning of the simulation when particles consist of isolated or a few aggregated monomers. For larger residence times the aggregation reaches the DLCA under near continuum flow regime. This simultaneous evolution of aggregation/flow regimes has important consequences on the aggregation kinetics, particle size distribution, and particle morphology to be further discussed in the following sections.
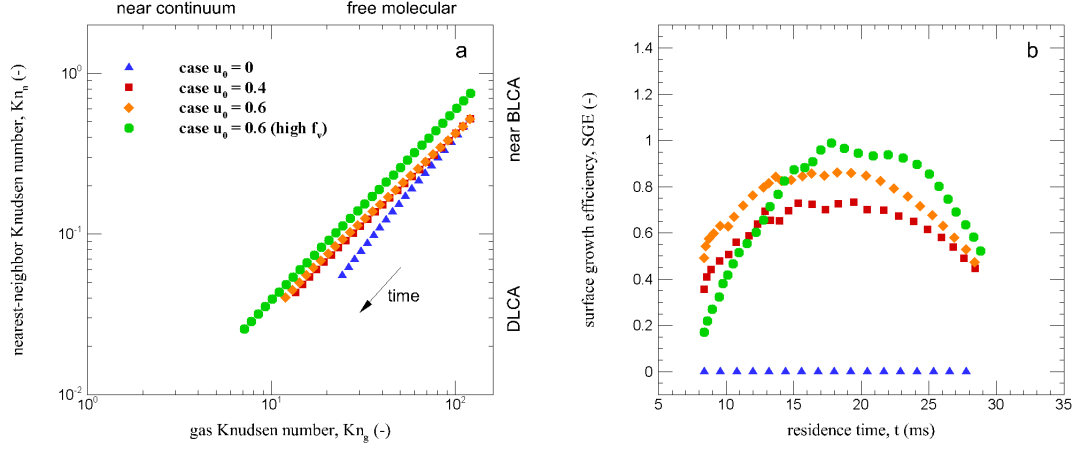
Figure 3: Simultaneous change in flow and aggregation regimes and surface growth efficiency.

4.2. Surface Growth Efficiency

A new dimensionless parameter called surface growth efficiency (SGE) is introduced in order to quantify the competition between aggregation and surface growth during the particle formation process,

$$\text{SGE} = \frac{\tau_a}{\tau_{sg}} \tag{5}$$

where $\tau_a = 2/(kn)$ and $\tau_{sg} = d_p/(6u)$ correspond to the time needed to duplicate the mass of particles by aggregation and surface growth, respectively. k is the monodisperse collision kernel, n the particle number concentration, and d_p is the average primary particle diameter (please see Appendix B). In this context, when SGE $\longrightarrow 0$ means that surface growth process is very slow compared to aggregation. On the other hand, SGE $\longrightarrow \infty$ means that surface growth is much faster and therefore more effective than aggregation in duplicating the mass of particles. Note that definitions with the same spirit have been introduced in previous works (Park & Rogak (2004); Binder et al. (2006); Al Zaitone et al. (2009)).

Fig. 3b presents the SGE as a function of time for all the simulated cases. For case $u_0 = 0$ the value is constant and equal to zero since no surface growth is considered. Cases with $u > 0$ show a similar time evolution by attaining a maximum value. This behavior is due to the fact that both τ_{sg} and τ_a are increasing in time in a competitive way. At the beginning of the simulation, SGE is proportional to the surface growth rate, excepting for the case with high f_v which promotes the aggregation efficiency. But surprisingly, when comparing both low and large volume fractions at the same growth rate ($u_0 = 0.6$), it appears that initially larger f_v will produce lower surface growth efficiency. However at a residence time ~ 20 ms the opposite behavior is observed. This indicates that surface growth is more efficient compared to aggregation when acting on already formed clusters. Considering that both cases have the same τ_{sg}, this behavior is explained by the faster increase in τ_a as a function of time for the case $u_0 = 0.6$ (high f_v). This phenomenon leads

10

SGE for the case $u_0 = 0.6$ (high f_v) to cross the cases $u_0 = 0.4$ and $u_0 = 0.6$ (low f_v) at times around $10 - 15$ ms.

4.3. Particle volume fraction and aggregation kinetics

Fig. 4a shows the evolution of the particle volume fraction as a function of time. For the case $u_0 = 0$ it remains constant in time since there is no mass transfer between particles and gas species. Cases with $u > 0$ show different levels of increase corresponding to different surface growth rates in time. Although cases $u_0 = 0.6$ under low and high f_v seems very different, their percentual increase in f_v relative to the beginning of the simulation is approximately the same (a factor of ~ 10) meanwhile the case with $u_0 = 0.4$ increase by a factor of ~ 7. This shows that the overall relative variation of the volume fraction is more sensitive to the surface growth rate evolution compared to the initial volume fraction.
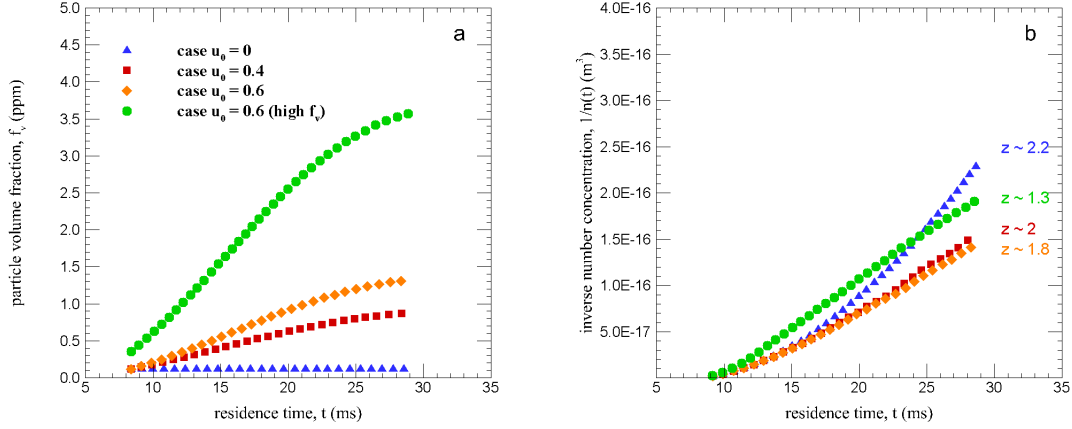

Figure 4: Time evolution of particle volume fraction and the inverse of the number concentration. Kinetc exponents are reported for $t \to 30$ ms.

Fig. 4b shows the time evolution of the inverse of the particle number concentration. Its slope in log-log plot is the kinetic exponent (z) indicating the collision and thus aggregation efficiency. In consequence, it is larger at short times for the case having high volume fraction whereas other cases report similar trends up to approximately 15 ms. However, for larger times ($t \to 30$ ms, kinetic exponents are reported in the figure) a considerable impact on the aggregation kinetics is observed. It is observed when comparing cases with $u_0 = 0.4$ and $u_0 = 0.6$ (low f_v) with the case without surface growth ($u_0 = 0$). Case $u_0 = 0.6$ (high f_v) shows a different evolution from the very beginning, where the aggregation is much more ballistic than other cases. Conversely, for large residence times, it has a lower kinetic exponent than other cases because it becomes much diffusive at the end of the simulation (see Fig. 3a). Indeed, surface growth makes the particles increase in mass and thus less mobile, which seems more important in terms of collision frequency

11

than the increase in particle collision radius. This would not be the case in pure free molecular flow regime where collision radius predominates over mobility. This shows the importance of considering the change in the flow regime (see Fig. 3a).

4.4. Primary particle coordination number

Fig. 5a shows in symbols the time evolution of the population average particle coordination number (Brasil et al. (2001)). Even in the absence of surface growth this parameter is increasing in time due to aggregation and its evolution can be accurately predicted by: $\overline{n_{c,\min}} = 2(N_p - 1)/N_p$ as introduced in section 2.3 (this is represented by a continuous line for each case in this figure). We can note that $\overline{n_{c,\min}}$ increase is moderated compared to $\overline{n_c}$ and not very dependent on the simulated case, excepting case $u_0 = 0.6$ (high f_v) showing $\overline{n_{c,\min}}$ to increase faster. For large residence times $\overline{n_{c,\min}}$ asymptotically tends towards 2 for all cases. This value is explained by the nature of cluster-cluster aggregation regardless of the primary particle polydispersity (Brasil et al. (2001); Lattuada et al. (2003); Yon et al. (2020)).

Note that case $u_0 = 0.6$ (high f_v) is the most ballistic at the beginning of the simulation and thus, a faster increase in $\overline{n_c}$ may be linked to larger fractal dimensions as observed by Weber & Friedlander (1997). However, when plotting $\overline{n_c}$ as a function of $\overline{N_p}$ (see Fig. S2 in the Supporting Material), it is not larger than other cases at equivalent $\overline{N_p}$. This suggests that aggregate compacity as revealed by fractal dimension is not the main cause of the observed faster increase in $\overline{n_c}$ as it will be confirmed in section 4.7. In turn, the more ballistic aggregation regime makes the aggregation faster at the beginning of the simulation, explaining the faster increase in $\overline{n_c}$ (and also in $\overline{n_{c,\min}}$).

On the other hand, $\overline{n_c}$ attains a maximum value between 1.9 to 8. Difference between $\overline{n_c}$ and $\overline{n_{c,\min}}$ is governed by the SGE (Fig. 3b), showing the importance of surface growth mechanism in the local compacity of particles. Local n_c (for individual monomers) can be as high as 16 as shown in Fig. 5(c1-c4). This can be observed in detail in Fig. S3 in the Supporting Material, reporting the distribution of n_c at the end of the simulation. Due to the observed large magnitudes of coordination numbers, we strongly recommend not neglecting the multi-sphere intersections to calculate the volume and surface area of aggregates consisting of overlapped monomers (when $u > 0$). Indeed, the difference $\overline{n_c} - \overline{n_{c,\min}}$ plays an important role for the particle's volume and surface area evaluation.

4.5. Primary particle overlapping coefficient

Fig. 5b presents the time evolution of the average overlapping coefficient ($\overline{c_{ov}}$) between primary particles (Oh & Sorensen (1997); Brasil et al. (1999)). This is calculated for each pair of intersecting primary particles of radii r_i and r_j, having a distance between centers d_{ij} as $c_{ov} = (r_i + r_j - d_{ij})/(r_i + r_j)$. When particles are point-touching then $d_{ij} = r_i + r_j$ and $c_{ov} = 0$, on the other hand when particles are completely fused then $d_{ij} = 0$ and $c_{ov} = 1$. In this context, when particles experience surface growth their radii is
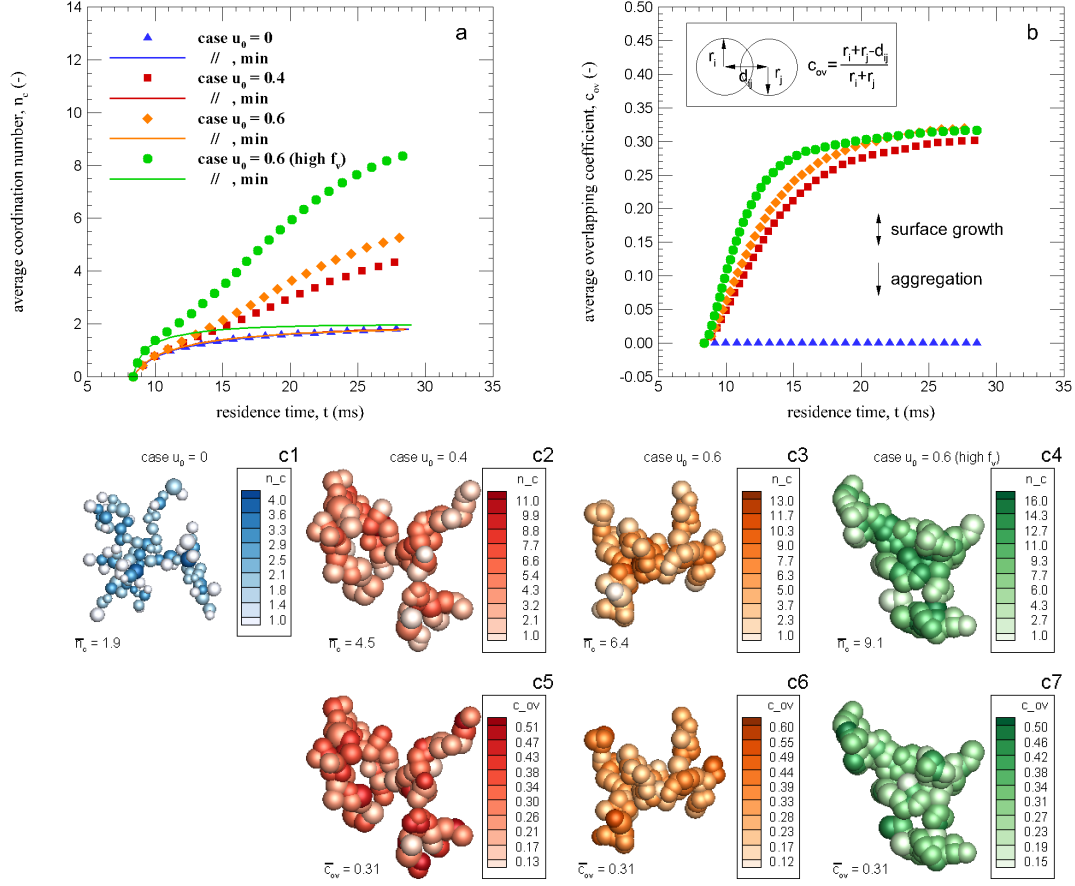
Figure 5: Time evolution of the average overlapping coefficient and coordination number. Continuous lines correspond to the minimum coordination number $\overline{n_{c,\min}}$ for each case. Examples of aggregates highlighting (by the color bar) the local coordination number (Figs. c1 - c4), and average overlapping coefficient per primary particle (Figs. c5 - c7).

continuously increasing in time which leads to an increasing overlap with neighbors. The local degree of overlapping depends consequently on the residence time that particles have been in contact under surface growth meanwhile, the average value for an individual aggregate depends also on the frequency of collisions with other particles (aggregation). Indeed, the latter tend to decrease the average overlapping coefficient. Additionally, surface growth plays a twofold and less evident role on $\overline{c_{ov}}$ to be explained as follows. Within an aggregate, the increase of monomers radii increases the overlapping with touching neighbors but also induces new intersections with monomers belonging to the same aggregate. These new internal-intersections consequently decrease $\overline{c_{ov}}$. Finally, it is due to these 3 aforementioned factors that the average overlapping coefficient attains a quite robust value around 30% for cases with $u > 0$ even though they have different levels of surface growth and aggregation/flow regimes. However, as shown in Fig. 5(c5-c7) local values of c_{ov}

13

(averaged over each individual primary particle) may be as high as 60% (see the case with $u_0 = 0.4$ under low f_v). This can be observed in detail in Fig. S4 in the Supporting Material, reporting the distribution of c_{ov} at the end of the simulations.

Experimental measurements of c_{ov} from TEM image analysis can only access to a 2d projected value $c_{ov,p}$. This is commonly measured on the periphery of the clusters where overlapping is visible and primary particle are clearly identifiable. It has been found to be within $c_{ov,p} = 0.11 - 0.29$ for Diesel soot (Wentzel et al. (2003)), within $c_{ov,p} = 0.13 - 0.30$ for soot from diffusion flames (Bourrous et al. (2018)). Particularly for ethylene diffusion flames it has been found to vary within the $c_{ov,p} = 0.26 - 0.36$ range for aged soot at different oxygen indices (Cortés et al. (2018)) and more recently within the $c_{ov,p} = 0.20 - 0.22$ range for aged soot from an ethylene premixed flame (Altenhoff et al. (2020)). Overall, these values are in good agreement with our numerical simulations.

4.6. Primary particle and aggregate size distributions

Considering Eq. (2), for cases with $u > 0$ the primary particle size distribution experiences an uniform shift towards larger values in time. The geometric mean primary particle diameter increases from the initial value of $d_p = 8$ nm up to 18 nm for the case $u_0 = 0.4$, and up to 21.5 nm for cases $u_0 = 0.6$ (please see Fig. S5a in the Supporting Material). However, this results in a decrease of the corresponding geometric standard deviation ($\sigma_{p,g}$) as reported in Fig. 6a whereas the standard deviation is time-invariant for all cases. Since, the only way to keep a geometric standard deviation constant is to shift the distribution in log scale, a shift in normal scale necessarily causes a decrease of the geometric standard deviation. This decrease of $\sigma_{p,g}$ has not been found by Kelesidis et al. (2017). We expect this discrepancy to be explained by the different ways to simulate the evolution of primary particle radii in the present study (Eq. 2). While Kelesidis et al. (2017) considered a monomer size dependent surface growth rate, in the present work all the primary particles grow at the same rate (under the hypothesis of a uniform flux density). This decrease in $\sigma_{p,g}$ is governed by the surface growth rates presented in Fig. 2. Obviously, in the case $u = 0$, it remains constant in time. The present study tends to conclude that surface growth reduces the geometric standard deviation of the primary particle diameter. Note that considering other mechanisms of soot formation, such as oxidation could lead to a different $\sigma_{p,g}$ evolution (Yon et al. (2018)).

On the other hand, the geometric mean volume-equivalent aggregate diameter increases from the initial value of 8 nm up to 26, 50, 57, and 90 nm for cases $u_0 = 0$, $u_0 = 0.4$, $u_0 = 0.6$, and $u_0 = 0.6$ (high f_v), respectively (please see Fig. S5b in the Supporting Material). Fig. 6b shows the time evolution of the corresponding aggregate geometric standard deviation $\sigma_{g,dv}$. Aggregation mechanism increases $\sigma_{g,dv}$ during time, with a maximum asymptotic value reached in the absence of surface growth ($u = 0$). This asymptotic value depends on the aggregation/flow regime (Morán et al. (2020b)). Conversely, surface growth tends
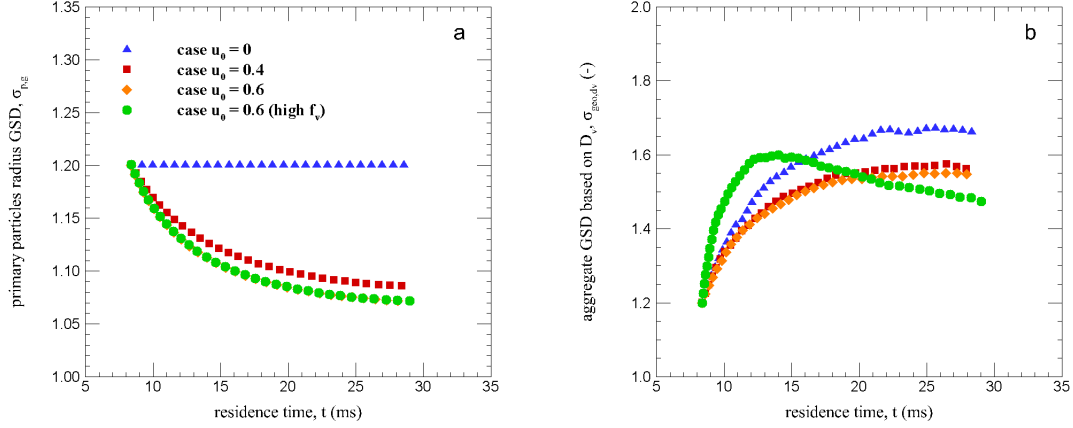
Figure 6: Time evolution of the geometric standard deviation (number-based) of primary particles and aggregate volume equivalent diameter.

to limit the increase in $\sigma_{g,dv}$, being consistent with previous works (Mountain et al. (1986); Tsantilis & Pratsinis (2004); Kelesidis et al. (2017)). This is attributed to the fact that larger aggregates experience a larger increase in mass due to surface growth however, they are also characterized by larger levels of overlapping and larger n_c which tends to decrease the population of larger particles and thus the geometric standard deviation. This may be the reason why for case $u_0 = 0.6$ (high f_v) the attained $\sigma_{g,dv}$ at $t = 30$ ms is the smallest among all simulated cases. This case is indeed the most diffusive at the end of the simulation (see Fig. 3a), consequently having a lower $\sigma_{g,dv}$ is expected. This because $\sigma_{g,dv}$ has been observed to be smaller for diffusive/transition than ballistic aggregation regimes (Morán et al. (2020b)).

Table 1: Aggregate geometric standard deviation (number-based) at the end of the simulation ($t = 30$ ms).

Case	$\sigma_{g,dm}$	$\sigma_{g,dg}$	$\sigma_{g,dv}$
$u_0 = 0$	1.77	2.23	1.63
$u_0 = 0.4$	1.70	2.00	1.57
$u_0 = 0.6$	1.61	1.85	1.49
$u_0 = 0.6$ (high f_v)	1.56	1.79	1.45

In addition, Table 1 shows the values of $\sigma_{g,dm}$ (based on the mobility diameter), $\sigma_{g,dg}$ (based on the gyration diameter), and $\sigma_{g,dv}$ calculated at $t = 30$ ms. For the case with $u = 0$, these values are in good agreement with Morán et al. (2020b). Also, these results are in good agreement with experimental measurements. Indeed, for aged soot particles sampled in an ethylene premixed flame, Altenhoff et al. (2020) found $\sigma_{g,dg}$ between 1.82 and 1.87 based on different methods to determine d_g from TEM image analysis.

Additionally, for aged soot particles from rich premixed ethylene flames studied by Maricq et al. (2003) found $\sigma_{g,dm} \sim 1.6$ from SMPS measurements. Also the SMPS measurements of Zhao et al. (2003) confirmed $\sigma_{g,dm}$ for aged soot particles to be between 1.50 to 1.64.

4.7. Particle morphology

Finally, in order to evaluate the impact of the surface growth/aggregation competition on the individual particle's morphology, we report (in symbols) in Fig. 7 the volume-based normalized pair correlation function for a set of representative aggregates. This function quantifies the probability to find some material at a certain distance r from a given point in the aggregate:

$$A(\overrightarrow{r}) = \int_{\overrightarrow{u}=\overrightarrow{0}}^{\infty} n(\overrightarrow{r} - \overrightarrow{u}) \, n(\overrightarrow{u}) \, d\overrightarrow{u} \tag{6}$$

where n report the presence of material at a given position $\overrightarrow{r}$ in the 3D space. It is numerically determined by calculating the exact volume of intersection between the aggregate and an identic copy which is shifted randomly in a 3-dimensional space (Morán et al. (2019)). $A(0)$ corresponds to the aggregate volume. The morphological information is contained in the radial dependence of $A(r)$ and thus, we report here the normalized expression of that function. This volume is calculated by using the SBL library (Cazals et al. (2011)). A total of 300 orientations and 200 radial positions (logarithmically spaced) are considered for all the aggregates studied as done in (Morán et al. (2019); Yon et al. (2020)).

As recently suggested by Yon et al. (2020), $A(r)$ consists of two components such that: $A(r) = A_{pp} + A_{agg}$, where A_{pp} is the contribution of primary particles to the aggregate morphology (self-intersection of primary particles), and A_{agg} is the contribution of the aggregate structure by considering the intersection between neighbor spheres. A_{pp} dominates at small scales, namely $r \to r_{p,v}$ (where $r_{p,v}$ is the monomer average volume-equivalent radius) whereas A_{agg} becomes predominant for larger scales. Fig. 7 shows an increase in the region governed by A_{pp} when increasing u, and a less evident hump at the transition between A_{pp} and A_{agg} is observed. Thus, in both figures surface growth makes it very difficult to dissociate their contribution to the total pair correlation function, especially when $u_0 = 0.6$. This also evidences that larger structures are needed to observe a well-established fractal (self-similar) behavior in $A(r)$. This is remarkably similar to increasing the primary particle polydispersity where also larger monomers are in competition with the scale of the aggregate in terms of volume and subsequently, A_{pp} cannot be easily differentiated from A_{agg} (Morán et al. (2019); Yon et al. (2020)).

Similarly to Yon et al. (2020), we attempt to fit the so determined pair correlation function based on the following model,

$$A_{pp}(r) = \left(1 + \frac{r}{4\widetilde{r_{p,v}}}\right)\left(1 - \frac{r}{2\widetilde{r_{p,v}}}\right)^2, \qquad r \in [0, 2\widetilde{r_{p,v}}] \tag{7a}$$

$$A_{agg}(r) = \frac{\varphi D_f}{3}\left(\frac{r}{r_{p,v}}\right)^{D_f - 3}\left[e^{-(r/\xi_{max})^\beta} - e^{-(r/\xi)^\beta}\right], \qquad r > 0 \tag{7b}$$

16

In this context, the packing factor φ, the individual fractal dimension D_f, the maximum and equivalent length scales ξ_{max} and ξ, respectively, the stretching exponent β and the volume-equivalent primary particle radius $\widetilde{r_{p,v}}$ are the fitted parameters. Please note that this model has not been rigorously adapted to overlapped spheres. This could alter the expression of A_{pp} and A_{agg} at small scales. In the present study, we focus on φ and D_f which are found at large scales and thus expected to be physically meaningful. A direct fit of all the aforementioned parameters is quite challenging and therefore a *fit-by-parts* procedure is proposed as thoroughly explained in page 8 of the Supporting Material.

A total of 2 aggregates per condition (sampled at the end of the simulations $t = 30$ ms) are fitted. They are selected according to N_p (within the $100 - 105$ range in Fig. 7a, and within the $430 - 450$ range in Fig. 7b). These aggregates are also selected for having representative anisotropy coefficients (A_{13}), where the most probable values are within the $1.7 - 4.0$ range (please see Fig. S6 in the Supporting Material). When analyzing the fitted parameters (reported in the figures), a significant increase in the packing factor φ is found when increasing u_0. The packing factor expresses the local compacity at the scale of primary particles (Heinson et al. (2012); Yon et al. (2020)). Note that the obtained φ values for the cases with $u_0 = 0$ are slightly different from those reported by Yon et al. (2020) where DLCA aggregates under the Epstein flow regime were simulated, while in the present study the change in aggregation/flow regimes is taken into account. It appears that surface growth increases that local compacity. This is explained by the increase in overlapping coefficient and coordination number as previously discussed. The effect of volume fraction seems to be of second-order since the two cases with $u_0 = 0.6$ at low and high volume fractions exhibit similar $A(r)$ curves.

The individual fractal dimensions determined during the fitting procedure are also reported in the figures. For aggregates consisting of $N_p = 100 - 105$, as shown in Fig. 7a, a fractal dimension can only be confidently found for the case $u = 0$. On the other hand, as shown in Fig. 7b, because the aggregates are larger, the individual fractal dimension can be robustly determined for each case. Except for the case $u_0 = 0.6$ (high f_v), it seems that the fractal structure of aggregates, as described by D_f, is not considerably affected by surface growth. The fractal dimension for the case $u_0 = 0.6$ (high f_v) is larger. This particular case has been shown to experience a more ballistic aggregation at the beginning of the simulation, consequently explaining the observed larger fractal dimension. In consequence, the morphology of the particles is affected by surface growth in the sense that the packing factor is increased (which may be related to the increase in the fractal prefactor (Yon et al. (2020)) but the fractal dimension seems not really sensitive to the surface growth itself. It is however strongly dependent on the change of aggregation regime as previously observed (Morán et al. (2020b)).
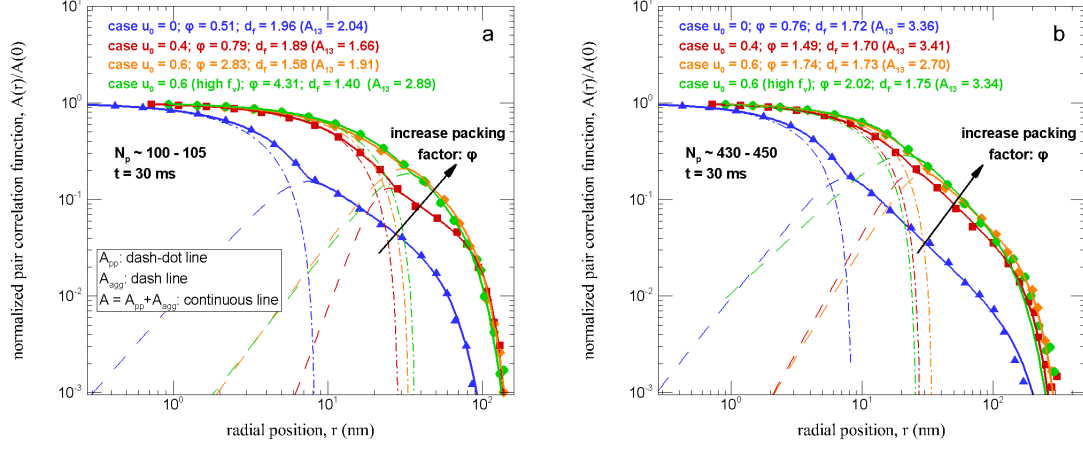
Figure 7: The symbols correspond to the normalized pair correlation function of aggregates with representative anisotropy and sampled at the end of the simulations ($t = 30$ ms). Aggregates made of $N_p \in [100, 105]$ and $N_p \in [430, 450]$ are reported on Fig. a and b, respectively. Continuous lines present the total fitted $A(r) = A_{pp} + A_{agg}$, while the two components A_{pp} and A_{agg} are the contribution of primary particles (dash-dot lines) and aggregate (dashed lines), respectively. Anisotropy coefficient A_{13}, and the fitted parameters (φ and D_f) are reported in the legends.

5. Conclusions

The simultaneous aggregation and surface growth of soot particles formed in an ethylene premixed flame is numerically simulated. Surface growth plays an important role in both particle aggregation and flow regime. Indeed, the added mass tends to reduce the particle mobility and subsequently slows down aggregation at large residence times. Also, it is found to decrease both the aggregate and primary particle geometric standard deviations.

In the present study, the competition between surface growth and aggregation mechanisms during time is quantified by introducing a new dimensionless parameter called the Surface Growth Efficiency. This parameter seems well correlated with the average primary particle coordination number (accounting for the number of intersections for monomer with nearest-neighbors). This parameter, commonly overlooked in the literature, is found to increase in time. For individual monomers, it can increase up to 16 while the global average attains a non-asymptotic maximum value between 4 to 8. This evidences that multi-sphere intersections should not be neglected when studying the physical properties of these types of aggregates, notably their volume and surface area.

According to the increase of the number of primary particle in contact, the local overlapping coefficient can be as high as 60% (depending on the surface growth rates and particles residence time), even though the global average values attain an asymptotic value around 30% irrespective of the Surface Growth Efficiency, in good accordance with experimental observations.

18

The morphological effect of surface growth is also studied by calculating the pair correlation function of individual aggregates representative of each case studied. The local compacity of aggregates, as quantified by the packing factor, considerably increases with Surface Growth Efficiency. This is linked to the increase in primary particles overlapping and coordination number. In addition, the analysis of large aggregates (consisting of ~ 440 monomers) reveals that individual fractal dimension is not strongly affected by surface growth and thus may be more sensitive to the change in aggregation regime (Morán et al. (2020b)).

In order to accurately simulate the competition between aggregation and surface growth, it is necessary to evaluate the volume of highly overlapped primary particles. This is particularly challenging when the coordination number is larger than the introduced minimum bound as shown in this work. Exact methods exist, such as ARVO (Buša et al. (2005)) or SBL (Cazals et al. (2011)) but they are too much expensive in terms of CPU time for being systematically integrated in a code aiming at simulating soot formation in flames, such as MCAC used here. For this reason, a semi-analytical method is proposed taking into account the multi-spheres intersection. The latter is commonly neglected in the literature (Brasil et al. (1999); Morán et al. (2018); Lindberg et al. (2019a)). The proposed determination of aggregate volume and surface area is shown to be very dependent on the coordination number $\overline{n_c}$ and more precisely to its difference with the minimum bound $\overline{n_{c,\min}}$. The proposed method can be potentially integrated in population balance (Eaves et al. (2016)), Monte Carlo (Lindberg et al. (2019b)) simulations, and may also improve experimental measurements of particle volume and surface area based on TEM image analysis (Wentzel et al. (2003); Bau et al. (2010); Bourrous et al. (2018); Ouf et al. (2019b)).

The updated version of the Monte Carlo Aggregation Code (MCAC) is available under the following website `https://gitlab.coria-cfd.fr/MCAC/MCAC`. In the future, soot particle nucleation and oxidation (fragmentation) will be also incorporated to this code.

Acknowledgments

Appendix A. Derivation of volume and surface area correction factors

Appendix A.1. Monodisperse primary particles, without multi-sphere intersection

As proposed by Morán et al. (2018) the volume v and surface area s can be calculated based on the concept of spherical caps formed at the intersection of spherical primary particles,

$$v = \sum_i^{N_p} \frac{4\pi}{3} r_i^3 - \sum_{(i,j)\in I} \frac{\pi}{3} \left[h_i^2 (3r_i - h_i) + h_j^2 (3r_j - h_j) \right] \tag{A.1a}$$

$$s = \sum_i^{N_p} 4\pi r_i^2 - \sum_{(i,j)\in I} 2\pi \left[r_i h_i + r_j h_j \right] \tag{A.1b}$$

Where I is the set of intersections between all pairs of primary particles (i,j) belonging to the same aggregate. The first term on the right hand side corresponds to the total volume or surface area of the spherical primary particles considered isolated. The second term is the discount of volume and surface, respectively, described as spherical caps of height h_i and radius r_i. When the primary particles are monodisperse in size these equations can be reduced as follows:

$$v = \frac{4\pi}{3} r_i^3 \times N_p - \sum_{i\in I} \frac{2\pi}{3} \left[h_i^2 (3r_i - h_i) \right] \tag{A.2a}$$

$$s = 4\pi r_i^2 \times N_p - \sum_{i\in I} 4\pi r_i h_i \tag{A.2b}$$

The overlapping coefficient for a pair of spheres is calculated as (Brasil et al. (1999); Morán et al. (2018)):

$$c_{ij} = \frac{r_i + r_j - d_{ij}}{r_i + r_j} \tag{A.3}$$

For monodisperse monomers it is reduced to $c_i = (2r_i - d)/(2r_i)$. Additionally, the spherical caps height can be written as $h_i = c_i r_i$. Replacing in eq. (A.2) the spherical caps height in terms of the overlapping coefficient the following expression is obtained:

$$v = \frac{4\pi}{3} r_i^3 \times N_p - \sum_{i\in I} \frac{4\pi}{3} r_i^3 \left[\frac{1}{2} c_i^2 (3 - c_i) \right] \tag{A.4a}$$

$$s = 4\pi r_i^2 \times N_p - \sum_{i\in I} 4\pi r_i^2 c_i \tag{A.4b}$$

The limitation of these equations is the inexplicit set of monomer intersections I. To overcome this issue we define the average coordination number as follows:

$$\overline{n_c} = \frac{1}{N_p} \sum_{i=1}^{N_p} n_{c,i} \tag{A.5}$$

Where $n_{c,i}$ is the coordination number of the ith primary particle, i.e. the number of intersections with neighbour monomers. Actually the total number of intersection is therefore $\overline{n_c} \times N_p/2$ corresponding to the magnitude of the set I. Then replacing in Eq. (A.4),

$$v = \frac{4\pi}{3} r_i^3 \times N_p - \frac{\overline{n_c} \times N_p}{2} \frac{4\pi}{3} r_i^3 \left[\frac{1}{2}(3c_{20}^2 - c_{30}^3) \right] \tag{A.6a}$$

$$s = 4\pi r_i^2 \times N_p - \frac{\overline{n_c} \times N_p}{2} 4\pi r_i^2 c_{10} \tag{A.6b}$$

Where the q-moment average overlapping coefficient is introduced as,

$$c_{q0} = \left[\frac{2}{\overline{n_c} N_p} \sum_{i=1}^{\overline{n_c} N_p/2} c_i^q \right]^{1/q} \tag{A.7}$$

Finally, dividing Eq. (A.6) by the first term on the right hand side the volume and surface area ratios are obtained,

$$\alpha_v = 1 - \frac{\overline{n_c}}{4}(3c_{20}^2 - c_{30}^3) \tag{A.8a}$$

$$\alpha_s = 1 - \frac{\overline{n_c}}{2} c_{10} \tag{A.8b}$$

Appendix A.2. Polydisperse primary particles, without multi-sphere intersection

Based on Morán et al. (2018) the volume v and surface area s can be calculated based on the spherical caps formed at the intersection of spherical primary particles:

$$v = \sum_i^{N_p} \frac{4\pi}{3} r_i^3 - \sum_{(i,j)\in I} \frac{1}{4} \left[\frac{4\pi}{3} r_i^3 \left(3\left(\frac{h_i}{r_i}\right)^2 - \left(\frac{h_i}{r_i}\right)^3 \right) + \frac{4\pi}{3} r_j^3 \left(3\left(\frac{h_j}{r_j}\right)^2 - \left(\frac{h_j}{r_j}\right)^3 \right) \right] \tag{A.9a}$$

$$s = \sum_i^{N_p} 4\pi r_i^2 - \sum_{(i,j)\in I} \frac{1}{2} \left[4\pi r_i^2 \left(\frac{h_i}{r_i}\right) + 4\pi r_j^2 \left(\frac{h_j}{r_j}\right) \right] \tag{A.9b}$$

Expressing the heights of the spherical caps in terms of the local overlapping coefficients $h_i = c_{ij}r_i$ and $h_j = c_{ij}r_j$:

$$v = \sum_i^{N_p} \frac{4\pi}{3}r_i^3 - \sum_{(i,j)\in I} \frac{1}{4} \left[\frac{4\pi}{3}r_i^3 \left(3\left(c_{ij}\right)^2 - \left(c_{ij}\right)^3 \right) + \frac{4\pi}{3}r_j^3 \left(3\left(c_{ij}\right)^2 - \left(c_{ij}\right)^3 \right) \right] \tag{A.10a}$$

$$s = \sum_i^{N_p} 4\pi r_i^2 - \sum_{(i,j)\in I} \frac{1}{2} \left[4\pi r_i^2 \left(c_{ij}\right) + 4\pi r_j^2 \left(c_{ij}\right) \right] \tag{A.10b}$$

Analogous to the case of monodisperse monomers the average coordination number is used to avoid using the inexplicit set of intersections I. Then dividing by the first term on the right hand side the following expressions for the volume and surface area ratios are obtained:

$$\alpha_v = 1 - \frac{\overline{n_c}}{4}\left(3c_{v,20}^2 - c_{v,30}^3\right) \tag{A.11a}$$

$$\alpha_s = 1 - \frac{\overline{n_c}}{2}c_{s,10} \tag{A.11b}$$

Where the q-moment volume and surface area average overlapping coefficients are thus introduced as follows:

$$c_{v,q0} = \left[\frac{1}{\sum_{i=1}^{\overline{n_c}N_p/2} \frac{4\pi}{3}r_i^3} \sum_{i=1}^{\overline{n_c}N_p/2} \frac{4\pi}{3}r_i^3 c_i^q \right]^{1/q} \tag{A.12a}$$

$$c_{s,q0} = \left[\frac{1}{\sum_{i=1}^{\overline{n_c}N_p/2} 4\pi r_i^2} \sum_{i=1}^{\overline{n_c}N_p/2} 4\pi r_i^2 c_i^q \right]^{1/q} \tag{A.12b}$$

Appendix A.3. Multi-sphere intersection correction factor

The spherical caps correction introduced before is valid if local intersection is limited at two spheres. Naturally, if the local coordination number exceeds 2, a correction must be added.

In consequence, the volume and surface area of particles are calculated based on the following factors:

$$\alpha_v = 1 - \frac{\overline{n_c}}{4}\left(3c_{v,20}^2 - c_{v,30}^3\right) + \beta_v \tag{A.13a}$$

$$\alpha_s = 1 - \frac{\overline{n_c}}{2}c_{s,10} + \beta_s \tag{A.13b}$$

where β_v and β_s as the volume and surface area correction factor given as follows,

$$\beta_v = a_v c_{v,30}^3 (\overline{n_c} - \overline{n_{c,\min}}) + b_v (\overline{n_c} - \overline{n_{c,\min}})^{1.5} \tag{A.14a}$$

$$\beta_s = a_s c_{s,10}^2 (\overline{n_c} - \overline{n_{c,\min}}) + b_s (\overline{n_c} - \overline{n_{c,\min}})^2 \tag{A.14b}$$

22

Where $\overline{n_{c,\min}} = 2(N_p - 1)/N_p$ is the minimum average coordination number. In these expressions a_v, b_v, a_s, and b_s are constants obtained by post-processing fits. In this context, for a given simulation of the simultaneous aggregation and surface growth (with $u_0 = 0.6$), Eq. (A.13) is fitted (by least-squeared) in post-processing to search the aforementioned parameters. This is achieved by comparison with α_v and α_s as determined by using the ARVO and SBL libraries (Buša et al. (2005); Cazals et al. (2011)). In this context, $a_v = 0.627418$, $b_v = 3.3245 \times 10^{-3}$, $a_s = 0.701325$, and $b_s = 4.5 \times 10^{-3}$ are obtained.
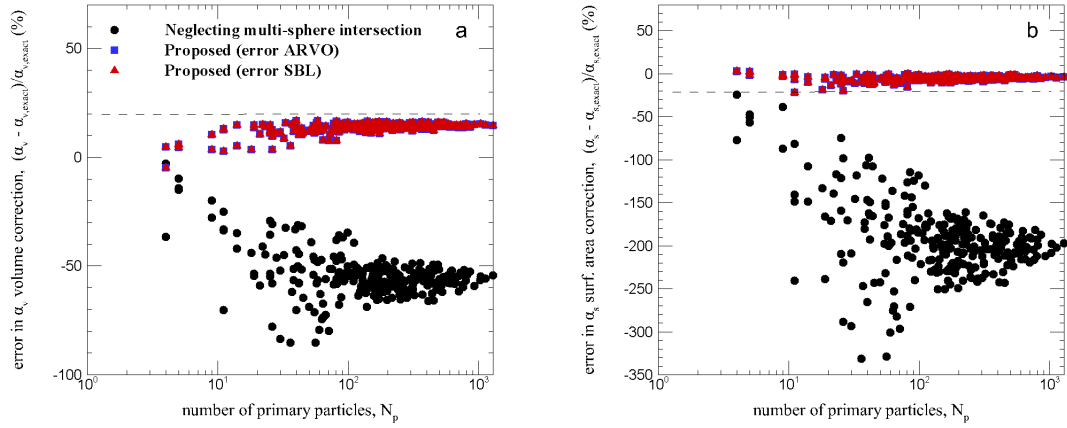

Figure A.8: Relative error on the proposed α_v and α_s correction factor for volume and surface area, respectively. Corresponding to case with $u_0 = 0.6$ (high f_v), evaluated at the end of the simulation ($t = 30$ ms).

Fig. A.8a and Fig. A.8b presents respectively the error on the volume and surface area correction factor when compared with ARVO (blue squared symbols) and SBL (red triangle symbols) libraries (Buša et al. (2005); Cazals et al. (2011)). The error when neglecting multi-sphere intersection is presented by black circles in both figures. The worst case in terms of maximum overlapping and coordination number is reported, i.e. $u_0 = 0.6$ (high f_v), evaluated at the end of the simulation ($t = 30$ ms). Both factors report an absolute error less than 20%. Note that error in α_v when neglecting multi-sphere intersection (neglecting β_v in Eq. A.13a) can goes up to 100%. In the same sense, the error in α_s when neglecting multi-sphere intersection (neglecting β_s in Eq. A.13b) can go below to -350%.

Appendix B. Derivation of the characteristic times of aggregation and surface growth

The characteristic time of aggregation can be obtained by integrating the population balance equation considering $n(t)$ the total number concentration which is not affected by surface growth.

$$\frac{dn(t)}{dt} = -\frac{1}{2}k_0[n(t)]^2 \tag{B.1}$$

the volume of particles (considered monodisperse) will be halved when the total number concentration is reduced by a factor of 2,

$$\int_{n_0}^{n_0/2} \frac{1}{n^2} \, dn = -\int_0^{\tau_a} \frac{1}{2} k_0 \, dt \tag{B.2}$$

Finally the following expression is obtained,

$$\tau_a = \frac{2}{k_0 n_0} \tag{B.3}$$

In addition, considering,

$$\frac{dv}{dt} = us \tag{B.4}$$

Then, the particle volume is be duplicated due to surface growth when,

$$\int_v^{2v} dv = \int_0^{\tau_{sg}} us \, dt \tag{B.5}$$

Finally, the following expression is obtained,

$$\tau_{sg} = \frac{d_p}{6u} \tag{B.6}$$

References

Abid, A. D., Heinz, N., Tolmachoff, E. D., Phares, D. J., Campbell, C. S., & Wang, H. (2008). On evolution of particle size distribution functions of incipient soot in premixed ethylene–oxygen–argon flames. *Combustion and Flame*, *154*, 775–788. doi:https://doi.org/10.1016/j.combustflame.2008.06.009.

Al Zaitone, B., Schmid, H.-J., & Peukert, W. (2009). Simulation of structure and mobility of aggregates formed by simultaneous coagulation, sintering and surface growth. *Journal of aerosol science*, *40*, 950–964. doi:https://doi.org/10.1016/j.jaerosci.2009.08.007.

Altenhoff, M., Aßmann, S., Teige, C., Huber, F. J., & Will, S. (2020). An optimized evaluation strategy for a comprehensive morphological soot nanoparticle aggregate characterization by electron microscopy. *Journal of Aerosol Science*, *139*, 105470. doi:https://doi.org/10.1016/j.jaerosci.2019.105470.

Appel, J., Bockhorn, H., & Frenklach, M. (2000). Kinetic modeling of soot formation with detailed chemistry and physics: laminar premixed flames of c2 hydrocarbons. *Combustion and flame*, *121*, 122–136. doi:https://doi.org/10.1016/S0010-2180(99)00135-2.

Balthasar, M., & Frenklach, M. (2005a). Detailed kinetic modeling of soot aggregate formation in laminar premixed flames. *Combustion and Flame*, *140*, 130–145. doi:https://doi.org/10.1016/j.combustflame.2004.11.004.

Balthasar, M., & Frenklach, M. (2005b). Monte-carlo simulation of soot particle coagulation and aggregation: the effect of a realistic size distribution. *Proceedings of the Combustion Institute*, *30*, 1467–1475. doi:https://doi.org/10.1016/j.proci.2004.07.035.

Bambha, R. P., & Michelsen, H. A. (2015). Effects of aggregate morphology and size on laser-induced incandescence and scattering from black carbon (mature soot). *Journal of Aerosol Science*, *88*, 159–181. doi:https://doi.org/10.1016/j.jaerosci.2015.06.006.

Bau, S., Witschger, O., Gensdarmes, F., Rastoix, O., & Thomas, D. (2010). A tem-based method as an alternative to the bet method for measuring off-line the specific surface area of nanoaerosols. *Powder Technology*, *200*, 190–201. doi:https://doi.org/10.1016/j.powtec.2010.02.023.

Betrancourt, C., Liu, F., Desgroux, P., Mercier, X., Faccinetto, A., Salamanca, M., Ruwe, L., Kohse-Höinghaus, K., Emmrich, D., Beyer, A. et al. (2017). Investigation of the size of the incandescent incipient soot particles in premixed sooting and nucleation flames of n-butane using lii, him, and 1 nm-smps. *Aerosol Science and Technology*, *51*, 916–935. doi:https://doi.org/10.1080/02786826.2017.1325440.

Binder, C., Feichtinger, C., Schmid, H.-J., Thürey, N., Peukert, W., & Rüde, U. (2006). Simulation of the hydrodynamic drag of aggregated particles. *Journal of colloid and interface science*, *301*, 155–167. doi:https://doi.org/10.1016/j.jcis.2006.04.045.

Bourrous, S., Ribeyre, Q., Lintis, L., Yon, J., Bau, S., Thomas, D., Vallières, C., & Ouf, F.-X. (2018). A semi-automatic analysis tool for the determination of primary particle size, overlap coefficient and specific surface area of nanoparticles aggregates. *Journal of Aerosol Science*, *126*, 122–132. doi:https://doi.org/10.1016/j.jaerosci.2018.09.001.

Brasil, A., Farias, T. L., & Carvalho, M. (1999). A recipe for image characterization of fractal-like aggregates. *Journal of Aerosol Science*, *30*, 1379–1389. doi:https://doi.org/10.1016/S0021-8502(99)00026-9.

Brasil, A., Farias, T. L., Carvalho, M. d. G., & Koylu, U. O. (2001). Numerical characterization of the morphology of aggregated particles. *Journal of Aerosol Science*, *32*, 489–508. doi:https://doi.org/10.1016/S0021-8502(00)00097-5.

Buša, J., Džurina, J., Hayryan, E., Hayryan, S., Hu, C.-K., Plavka, J., Pokornỳ, I., Skřivánek, J., & Wu, M.-C. (2005). ARVO: A fortran package for computing the solvent accessible surface area and the excluded volume of overlapping spheres via analytic equations. *Computer physics communications*, *165*, 59–96. doi:https://doi.org/10.1016/j.cpc.2004.08.002.

Camejo, M., Espeso, D., & Bonilla, L. (2014). Influence of primary-particle density in the morphology of agglomerates. *Physical Review E*, *90*, 012306. doi:https://doi.org/10.1103/PhysRevE.90.012306.

Cazals, F., Kanhere, H., & Loriot, S. (2011). Computing the volume of a union of balls: a certified algorithm. *ACM Transactions on Mathematical Software (TOMS)*, *38*, 1–20. doi:https://doi.org/10.1145/2049662.2049665.

Chen, D., Akroyd, J., Mosbach, S., & Kraft, M. (2015). Surface reactivity of polycyclic aromatic hydrocarbon clusters. *Proceedings of the Combustion Institute*, *35*, 1811–1818. doi:https://doi.org/10.1016/j.proci.2014.06.140.

Cortés, D., Morán, J., Liu, F., Escudero, F., Consalvi, J.-L., & Fuentes, A. (2018). Effect of fuels and oxygen indices on the morphology of soot generated in laminar coflow diffusion flames. *Energy & fuels*, *32*, 11802–11813. doi:https://doi.org/10.1021/acs.energyfuels.8b01301.

Deng, X., Huang, Z., Wang, W., & Davé, R. N. (2016). Investigation of nanoparticle agglomerates properties using monte carlo simulations. *Advanced Powder Technology*, *27*, 1971–1979.

Doner, N., Liu, F., & Yon, J. (2017). Impact of necking and overlapping on radiative properties of coated soot aggregates. *Aerosol Science and Technology*, *51*, 532–542. doi:https://doi.org/10.1080/02786826.2016.1275513.

D'Anna, A., Sirignano, M., & Kent, J. (2010). A model of particle nucleation in premixed ethylene flames. *Combustion and flame*, *157*, 2106–2115. doi:https://doi.org/10.1016/j.combustflame.2010.04.019.

Eaves, N. A., Zhang, Q., Liu, F., Guo, H., Dworkin, S. B., & Thomson, M. J. (2016). Coflame: A refined and validated numerical algorithm for modeling sooting laminar coflow diffusion flames. *Computer Physics Communications*, *207*, 464–477. doi:https://doi.org/10.1016/j.cpc.2016.06.016.

Eggersdorfer, M. L., Kadau, D., Herrmann, H. J., & Pratsinis, S. E. (2012). Aggregate morphology evolution by sintering: Number and diameter of primary particles. *Journal of aerosol science*, *46*, 7–19. doi:https://doi.org/10.1016/j.jaerosci.2011.11.005.

Frenklach, M. (1996). On surface growth mechanism of soot particles. In *Symposium (International) on Combustion* (pp. 2285–2293). Elsevier volume 26. doi:https://doi.org/10.1016/S0082-0784(96)80056-7.

Frenklach, M., & Wang, H. (1991). Detailed modeling of soot particle nucleation and growth. In *Symposium (International) on Combustion* (pp. 1559–1566). Citeseer volume 23. doi:https://doi.org/10.1016/S0082-0784(06)80426-1.

Gatoo, M. A., Naseem, S., Arfat, M. Y., Mahmood Dar, A., Qasim, K., & Zubair, S. (2014). Physicochemical properties of nanomaterials: implication in associated toxic manifestations. *BioMed research international*, *2014*. doi:https://doi.org/10.1155/2014/498420.

Gensch, M., & Weber, A. (2017). Rebound behavior of nanoparticle-agglomerates. *Advanced Powder Technology*, *28*, 1930–1942. doi:https://doi.org/10.1016/j.apt.2017.05.003.

Harris, S. J. (1984). Quantitative chemical mechanism for heterogeneous growth of soot particles in premixed flames. ACS Publications. doi:https://doi.org/10.1021/bk-1983-0249.ch002.

Harris, S. J. (1990). Surface growth and soot particle reactivity. *Combustion science and technology*, *72*, 67–77. doi:https://doi.org/10.1080/00102209008951640.

Harris, S. J., & Weiner, A. M. (1985). Chemical kinetics of soot particle growth. *Annual Review of Physical Chemistry*, *36*, 31–52. doi:https://doi.org/10.1146/annurev.pc.36.100185.000335.

Heinson, W., Sorensen, C., & Chakrabarti, A. (2012). A three parameter description of the structure of diffusion limited cluster fractal aggregates. *Journal of colloid and interface science*, *375*, 65–69. doi:https://doi.org/10.1016/j.jcis.2012.01.062.

Hou, D., Lindberg, C. S., Wang, M., Manuputty, M. Y., You, X., & Kraft, M. (2020). Simulation of primary particle size distributions in a premixed ethylene stagnation flame. *Combustion and Flame*, *216*, 126–135. doi:https://doi.org/10.1016/j.combustflame.2020.02.028.

Hussain, S., Boland, S., Baeza-Squiban, A., Hamel, R., Thomassen, L. C., Martens, J. A., Billon-Galland, M. A., Fleury-Feith, J., Moisan, F., Pairon, J.-C. et al. (2009). Oxidative stress and proinflammatory effects of carbon black and titanium dioxide nanoparticles: role of particle surface area and internalized amount. *Toxicology*, *260*, 142–149. doi:https://doi.org/10.1016/j.tox.2009.04.001.

Inci, G., Kronenburg, A., Weeber, R., & Pflüger, D. (2017). Langevin dynamics simulation of transport and aggregation of soot nano-particles in turbulent flows. *Flow, Turbulence and Combustion*, *98*, 1065–1085. doi:https://doi.org/10.1007/s10494-016-9797-3.

Isella, L., & Drossinos, Y. (2010). Langevin agglomeration of nanoparticles interacting via a central potential. *Physical Review E*, *82*, 011404. doi:https://doi.org/10.1103/PhysRevE.82.011404.

Johnsson, J., Bladh, H., Olofsson, N.-E., & Bengtsson, P.-E. (2013). Influence of soot aggregate structure on particle sizing using laser-induced incandescence: importance of bridging between primary particles. *Applied Physics B*, *112*, 321–332. doi:https://doi.org/10.1007/s00340-013-5355-z.

Kauffman, G. B. (2013). *Alfred Werner: Founder of Coordination Chemistry*. Springer Science & Business Media.

Kelesidis, G. A., Goudeli, E., & Pratsinis, S. E. (2017). Flame synthesis of functional nanostructured materials and devices: Surface growth and aggregation. *Proceedings of the Combustion Institute*, *36*, 29–50. doi:https://doi.org/10.1016/j.proci.2016.08.078.

Kwon, H.-S., Ryu, M. H., & Carlsten, C. (2020). Ultrafine particles: unique physicochemical properties relevant to health and disease. *Experimental & Molecular Medicine*, (pp. 1–11). doi:https://doi.org/10.1038/s12276-020-0405-1.

Lapuerta, M., Expósito, J. J., & Martos, F. J. (2015). Effect of sintering on the fractal prefactor of agglomerates. *Powder Technology*, *271*, 141–154. doi:https://doi.org/10.1016/j.powtec.2014.10.041.

Lattuada, M., Wu, H., & Morbidelli, M. (2003). A simple model for the structure of fractal aggregates. *Journal of colloid and interface science*, *268*, 106–120. doi:https://doi.org/10.1016/j.jcis.2003.07.027.

Lazzari, S., & Lattuada, M. (2017). Growth and aggregation regulate clusters structural properties and gel time. *The Journal of Physical Chemistry B*, *121*, 2511–2524. doi:https://doi.org/10.1021/acs.jpcb.6b12682.

Lindberg, C. S., Manuputty, M. Y., Akroyd, J., & Kraft, M. (2019a). A two-step simulation methodology for modelling stagnation flame synthesised aggregate nanoparticles. *Combustion and Flame*, *202*, 143–153. doi:https://doi.org/10.1016/j.combustflame.2019.01.010.

Lindberg, C. S., Manuputty, M. Y., Yapp, E. K., Akroyd, J., Xu, R., & Kraft, M. (2019b). A detailed particle model for polydisperse aggregate particles. *Journal of Computational Physics*, *397*, 108799. doi:https://doi.org/10.1016/j.jcp.2019.06.074.

Liu, F., Stagg, B. J., Snelling, D. R., & Smallwood, G. J. (2006). Effects of primary soot particle size distribution on the temperature of soot particles heated by a nanosecond pulsed laser in an atmospheric laminar diffusion flame. *International Journal of Heat and Mass Transfer*, *49*, 777–788. doi:https://doi.org/10.1016/j.ijheatmasstransfer.2005.07.041.

Maricq, M. M., Harris, S. J., & Szente, J. J. (2003). Soot size distributions in rich premixed ethylene flames. *Combustion and Flame*, *132*, 328–342. doi:https://doi.org/10.1016/S0010-2180(02)00502-3.

Melas, A. D., Isella, L., Konstandopoulos, A. G., & Drossinos, Y. (2014). Morphology and mobility of synthetic colloidal aggregates. *Journal of colloid and interface science*, *417*, 27–36. doi:https://doi.org/10.1016/j.jcis.2013.11.024.

Mitchell, P., & Frenklach, M. (1998). Monte carlo simulation of soot aggregation with simultaneous surface growth-why primary particles appear spherical. In *Symposium (International) on Combustion* (pp. 1507–1514). Elsevier volume 27. doi:https://doi.org/10.1016/S0082-0784(98)80558-4.

Mitchell, P., & Frenklach, M. (2003). Particle aggregation with simultaneous surface growth. *Physical Review E*, *67*, 061407. doi:https://doi.org/10.1103/PhysRevE.67.061407.

Morán, J., Cuevas, J., Liu, F., Yon, J., & Fuentes, A. (2018). Influence of primary particle polydispersity and overlapping on soot morphological parameters derived from numerical tem images. *Powder technology*, *330*, 67–79. doi:https://doi.org/10.1016/j.powtec.2018.02.008.

Morán, J., Fuentes, A., Liu, F., & Yon, J. (2019). FracVAL: An improved tunable algorithm of cluster–cluster aggregation for generation of fractal structures formed by polydisperse primary particles. *Computer Physics Communications*, *239*,

225–237. doi:https://doi.org/10.1016/j.cpc.2019.01.015.

Morán, J., Yon, J., & Poux, A. (2020a). Monte carlo aggregation code (MCAC) part 1: Fundamentals. *Journal of Colloid and Interface Science*, *569*, 184–194. doi:https://doi.org/10.1016/j.jcis.2020.02.039.

Morán, J., Yon, J., Poux, A., Corbin, F., Ouf, F.-X., & Siméon, A. (2020b). Monte carlo aggregation code (MCAC) part 2: Application to soot agglomeration, highlighting the importance of primary particles. *Journal of Colloid and Interface Science*, *575*, 274–285. doi:https://doi.org/10.1016/j.jcis.2020.04.085.

Morgan, N., Kraft, M., Balthasar, M., Wong, D., Frenklach, M., & Mitchell, P. (2007). Numerical simulations of soot aggregation in premixed laminar flames. *Proceedings of the Combustion Institute*, *31*, 693–700. doi:https://doi.org/10.1016/j.proci.2006.08.021.

Mountain, R. D., Mulholland, G. W., & Baum, H. (1986). Simulation of aerosol agglomeration in the free molecular and continuum flow regimes. *Journal of Colloid and Interface Science*, *114*, 67–81. doi:https://doi.org/10.1016/0021-9797(86)90241-9.

Oh, C., & Sorensen, C. (1997). The effect of overlap between monomers on the determination of fractal cluster morphology. *Journal of Colloid and Interface Science*, *193*, 17–25. doi:https://doi.org/10.1006/jcis.1997.5046.

Ono, K., Dewa, K., Matsukawa, Y., Saito, Y., Matsushita, Y., Aoki, H., Era, K., Aoki, T., & Yamaguchi, T. (2017). Experimental evidence for the sintering of primary soot particles. *Journal of Aerosol Science*, *105*, 1–9. doi:https://doi.org/10.1016/j.jaerosci.2016.11.013.

Ouf, F.-X., Bourrous, S., Fauvel, S., Kort, A., Lintis, L., Nuvoli, J., & Yon, J. (2019a). True density of combustion emitted particles: A comparison of results highlighting the influence of the organic contents. *Journal of Aerosol Science*, *134*, 1–13. doi:https://doi.org/10.1016/j.jaerosci.2019.04.007.

Ouf, F.-X., Bourrous, S., Vallières, C., Yon, J., & Lintis, L. (2019b). Specific surface area of combustion emitted particles: Impact of primary particle diameter and organic content. *Journal of Aerosol Science*, *137*, 105436. doi:https://doi.org/10.1016/j.jaerosci.2019.105436.

Park, S., & Rogak, S. (2004). A novel fixed-sectional model for the formation and growth of aerosol agglomerates. *Journal of Aerosol Science*, *35*, 1385–1404. doi:https://doi.org/10.1016/j.jaerosci.2004.05.010.

Patiño, F., Cruz, J., Verdugo, I., Morán, J., Consalvi, J., Liu, F., Du, X., & Fuentes, A. (2020). Soot primary particle sizing in a n-heptane doped methane/air laminar coflow diffusion flame by planar two-color tire-lii and tem image analysis. *Fuel*, *266*, 117030. doi:https://doi.org/10.1016/j.fuel.2020.117030.

Post, P., Bierwirth, M., & Weber, A. (2018). Mechanical stability measurements of surface modified nanoparticle agglomerates. *Journal of Aerosol Science*, *126*, 33–46. doi:https://doi.org/10.1016/j.jaerosci.2018.08.007.

Prakash, A., Bapat, A., & Zachariah, M. (2003). A simple numerical algorithm and software for solution of nucleation, surface growth, and coagulation problems. *Aerosol Science & Technology*, *37*, 892–898. doi:https://doi.org/10.1080/02786820300933.

Rumpf, H. (1958). Grundlagen und methoden des granulierens. *Chemie Ingenieur Technik*, *30*, 144–158. doi:https://doi.org/10.1002/cite.330300307.

Russo, C., Tregrossi, A., & Ciajolo, A. (2015). Dehydrogenation and growth of soot in premixed flames. *Proceedings of the Combustion Institute*, *35*, 1803–1809. doi:https://doi.org/10.1016/j.proci.2014.05.024.

Sager, T. M., & Castranova, V. (2009). Surface area of particle administered versus mass in determining the pulmonary toxicity of ultrafine and fine carbon black: comparison to ultrafine titanium dioxide. *Particle and fibre toxicology*, *6*, 15. doi:https://doi.org/10.1186/1743-8977-6-15.

Salenbauch, S., Sirignano, M., Pollack, M., D'Anna, A., & Hasse, C. (2018). Detailed modeling of soot particle formation and comparison to optical diagnostics and size distribution measurements in premixed flames using a method of moments. *Fuel*, *222*, 287–293. doi:https://doi.org/10.1016/j.fuel.2018.02.148.

Schmid, H.-J., Al-Zaitone, B., Artelt, C., & Peukert, W. (2006). Evolution of the fractal dimension for simultaneous coagulation and sintering. *Chemical engineering science*, *61*, 293–305. doi:https://doi.org/10.1016/j.ces.2004.11.068.

Schmid, O., & Stoeger, T. (2016). Surface area is the biologically most effective dose metric for acute nanoparticle toxicity in the lung. *Journal of Aerosol Science*, *99*, 133–143. doi:https://doi.org/10.1016/j.jaerosci.2015.12.006.

Sirignano, M., Bartos, D., Conturso, M., Dunn, M., D'Anna, A., & Masri, A. R. (2017). Detection of nanostructures and soot in laminar premixed flames. *Combustion and Flame*, *176*, 299–308. doi:https://doi.org/10.1016/j.combustflame.2016.10.009.

Stoeger, T., Schmid, O., Takenaka, S., & Schulz, H. (2007). Inflammatory response to tio2 and carbonaceous particles scales best with bet surface area. *Environmental health perspectives*, *115*, A290–A291. doi:https://doi.org/10.1289/ehp.115-a290b.

Sutcu, E., Doner, N., Liu, F., Ercetin, U., Sen, F., Yon, J., Morán, J., & Fuentes, A. (2020). Morphological and radiative characteristics of soot aggregates: Experimental and numerical research. *Scientific Reports*, *10*, 1–12. doi:https://doi.org/10.1038/s41598-019-57045-y.

Thajudeen, T., Deshmukh, S., & Hogan Jr, C. J. (2015). Langevin simulation of aggregate formation in the transition regime. *Aerosol Science and Technology*, *49*, 115–125. doi:https://doi.org/10.1080/02786826.2015.1008971.

Thajudeen, T., Gopalakrishnan, R., & Hogan Jr, C. J. (2012). The collision rate of nonspherical particles and aggregates for all diffusive knudsen numbers. *Aerosol Science and Technology*, *46*, 1174–1186. doi:https://doi.org/10.1080/02786826.2012.701353.

Tsantilis, S., & Pratsinis, S. E. (2004). Narrowing the size distribution of aerosol-made titania by surface growth and coagulation. *Journal of aerosol science*, *35*, 405–420. doi:https://doi.org/10.1016/j.jaerosci.2003.09.006.

Veshkini, A., Dworkin, S. B., & Thomson, M. J. (2014). A soot particle surface reactivity model applied to a wide range of laminar ethylene/air flames. *Combustion and flame*, *161*, 3191–3200. doi:https://doi.org/10.1016/j.combustflame.2014.05.024.

Weber, A. P., & Friedlander, S. K. (1997). Relation between coordination number and fractal dimension of aerosol agglomerates. *Journal of Aerosol Science*, *1001*, S765–S766. doi:https://doi.org/10.1016/S0021-8502(97)85381-5.

Wentzel, M., Gorzawski, H., Naumann, K.-H., Saathoff, H., & Weinbruch, S. (2003). Transmission electron microscopical and aerosol dynamical characterization of soot aerosols. *Journal of aerosol science*, *34*, 1347–1370. doi:https://doi.org/10.1016/S0021-8502(03)00360-4.

Wozniak, M., Onofri, F., Barbosa, S., Yon, J., & Mroczka, J. (2012). Comparison of methods to derive morphological parameters of multi-fractal samples of particle aggregates from tem images. *Journal of Aerosol Science*, *47*, 12–26. doi:https://doi.org/10.1016/j.jaerosci.2011.12.008.

Yon, J., Bescond, A., & Liu, F. (2015a). On the radiative properties of soot aggregates part 1: Necking and overlapping. *Journal of Quantitative Spectroscopy and Radiative Transfer*, *162*, 197–206. doi:https://doi.org/10.1016/j.jqsrt.2015.03.027.

Yon, J., Bescond, A., & Ouf, F.-X. (2015b). A simple semi-empirical model for effective density measurements of fractal aggregates. *Journal of Aerosol Science*, *87*, 28–37. doi:https://doi.org/10.1016/j.jaerosci.2015.05.003.

Yon, J., Morán, J., Ouf, F.-X., Mazur, M., & Mitchell, J. (2020). From monomers to agglomerates: A generalized model for characterizing the morphology of fractal-like clusters. *Journal of Aerosol Science*, *151*, 105628. doi:https://doi.org/10.1016/j.jaerosci.2020.105628.

Yon, J., Ouf, F.-X., Hebert, D., Mitchell, J. B., Teuscher, N., Garrec, J.-L. L., Bescond, A., Baumann, W., Ourdani, D., Bizien, T., & Perez, J. (2018). Investigation of soot oxidation by coupling lii, saxs and scattering measurements. *Combustion and Flame*, *190*, 441 – 453. doi:https://doi.org/10.1016/j.combustflame.2017.12.014.

Zahaf, R., Kim, S.-K., Shin, J., Park, K., Choi, T.-Y., & Lee, D. (2015). Effect of volume fraction on transient structural behavior of aerosol particles using off-lattice kinetic monte carlo simulation. *Aerosol Science and Technology*, *49*, 1242–1255. doi:https://doi.org/10.1080/02786826.2015.1116681.

Zhao, B., Yang, Z., Johnston, M. V., Wang, H., Wexler, A. S., Balthasar, M., & Kraft, M. (2003). Measurement and numerical simulation of soot particle size distribution functions in a laminar premixed ethylene-oxygen-argon flame. *Combustion and Flame*, *133*, 173–188. doi:https://doi.org/10.1016/S0010-2180(02)00574-6.

Supporting Material

Impact of the competition between aggregation and surface growth on the morphology of soot particles formed in an ethylene laminar premixed flame

José Morán, Alexandre Poux, and Jérôme Yon[*]

Normandie Univ., INSA Rouen, UNIROUEN, CNRS, CORIA, 76000, Rouen, France

*Corresponding author: yon@coria.fr

Macroscopic population balance simulations

Solving the population balance equation

The collision-based population balance equation (PBE) for an aerosol without experiencing surface growth, sintering, nucleation and fragmentation is given as follows (Friedlander (2000)),

$$\frac{dn(v)}{dt} = \frac{1}{2}\int_0^v \beta(v-\tilde{v},\tilde{v})n(v-\tilde{v})n(\tilde{v})\,d\tilde{v} - n(v)\int_0^\infty \beta(v,\tilde{v})n(\tilde{v})\,d\tilde{v} \tag{1}$$

Here $n(v)$ is the number concentration ($1/m^3$) of particles with volume v. In addition, $\beta(v-\tilde{v},\tilde{v})$ is the collision frequency (m^3/s) between particles with volume $(v-\tilde{v})$ and $\tilde{v}$. This equation is numerically solved based on the method proposed by Prakash $et\ al.$ (2003). In this context, the volume-based particle size distribution is discretized into θ nodes as,

$$\frac{dn_k}{dt} = \frac{1}{2}\sum_{i=1}^{\theta}\sum_{j=1}^{\theta}\chi_{ijk}\beta_{ij}n_in_j - n_k\sum_{i=1}^{\theta}\beta_{ik}n_i \tag{2}$$

Where two particles with volumes v_i and v_j collide with frequency β_{ij} to form a third one of volume $v_i + v_j$. To take into account that this volume may fall between two consecutive nodes, the size-splitting operator χ_{ijk} is determined as follows (Prakash $et\ al.$ (2003)),

$$\chi_{ijk} = \begin{cases} \dfrac{v_{k+1}-(v_i+v_j)}{v_{k+1}-v_k}; & \text{if } v_k \le v_i+v_j \le v_{k+1} \\ \dfrac{(v_i+v_j)-v_{k-1}}{v_k-v_{k-1}}; & \text{if } v_{k-1} \le v_i+v_j \le v_k \\ \qquad 0; & \text{otherwise} \end{cases} \tag{3}$$

Calculating the coagulation kernels

The method introduced by Thajudeen $et\ al.$ (2012) taking into account of the fractal-like structure of aggregates is used. For a pair of particles belonging to the node i and node j, the collision kernel is calculated as,

$$\beta_{ij} = \frac{f_{ij}R_{s,ij}}{m_{ij}\pi}g(\text{Kn}_\text{D}) \tag{4}$$

Where $f_{ij} = f_if_j(f_i+f_j)$ and $m_{ij} = m_im_j/(m_i+m_j)$ are the reduced friction coefficient and mass, respectively (f_i and m_i are the mass and friction coefficient of particles belonging to the node i). Also, $R_{s,ij}$ is the combined collision (or Smoluchowski) radius and $g = g(\text{Kn}_\text{D})$ is a function adapting the coagulation kernel for collisions in the diffusive, intermediate and ballistic regime depending on the diffusive Knudsen number Kn_D,

$$g(\text{Kn}_\text{D}) = \frac{4\pi\text{Kn}_\text{D}^2 + c_1\text{Kn}_\text{D}^3 + (8\pi)^{1/2}c_2\text{Kn}_\text{D}^4}{1 + c_3\text{Kn}_\text{D} + c_4\text{Kn}_\text{D}^2 + c_2\text{Kn}_\text{D}^3} \tag{5}$$

Where $c_1 = 25.836$, $c_2 = 11.211$, $c_3 = 3.502$ and $c_4 = 7.211$. Additionally, the diffusive Knudsen number $\text{Kn}_\text{D} = \left(k_B T m_{ij}\right)^{1/2}/(f_{ij}R_{s,ij})$. Where k_B is the Boltzmann constant and T is the temperature of particles (assumed in thermal equilibrium with the surrounding gas). Finally, the combined collision radius $R_{s,ij}$ is determined as follows,

$$R_{s,ij} = a_i\left[1.203 - \frac{0.4315(N_i + N_j)}{(N_i D_f + N_j D_f)}\right] \times \left(\frac{R_{s,i}}{a_i} + \frac{R_{s,j}}{a_j}\right)^{\left(0.8806 + \frac{0.3497(N_i + N_j)}{(N_i D_f + N_j D_f)}\right)} \tag{6a}$$

$$R_{s,i} = a_i \Phi_R \left(\frac{N_i}{k_f}\right)^{1/D_f} \tag{6b}$$

$$\Phi_R = \frac{1}{\alpha_1 \ln[N_i] + \alpha_2} \tag{6c}$$

$$\alpha_1 = 0.253 D_f^2 - 1.209 D_f + 1.433 \tag{6d}$$

$$\alpha_2 = -0.218 D_f^2 + 0.964 D_f - 0.180 \tag{6e}$$

Where a_i and N_i is the radius and number of primary particles per aggregate. D_f and k_f are the fractal dimension and prefactor, respectively. The latter are the parameters describing the morphology of aggregates and are considered constant throughout one simulation.

Results

Figure S4 present a comparison between this methodology with those simulations based on MCAC for the case where $u = 0$, i.e. no surface growth is considered. Relevant macroscopic properties are selected for comparison such as the particle number concentration, the average number of primary particles per aggregate, the aggregate volume-equivalent diameter geometric mean and standard deviation (GSD). A total of $\theta = 41$ nodes are considered for PBE simulations (Prakash *et al.* (2003)). Considering the uncertainty in the fractal dimension of PBE simulations, three different values are imposed, namely $D_f = 1.6$, 1.8 and 2.0. The agreement between both methods is acceptable.
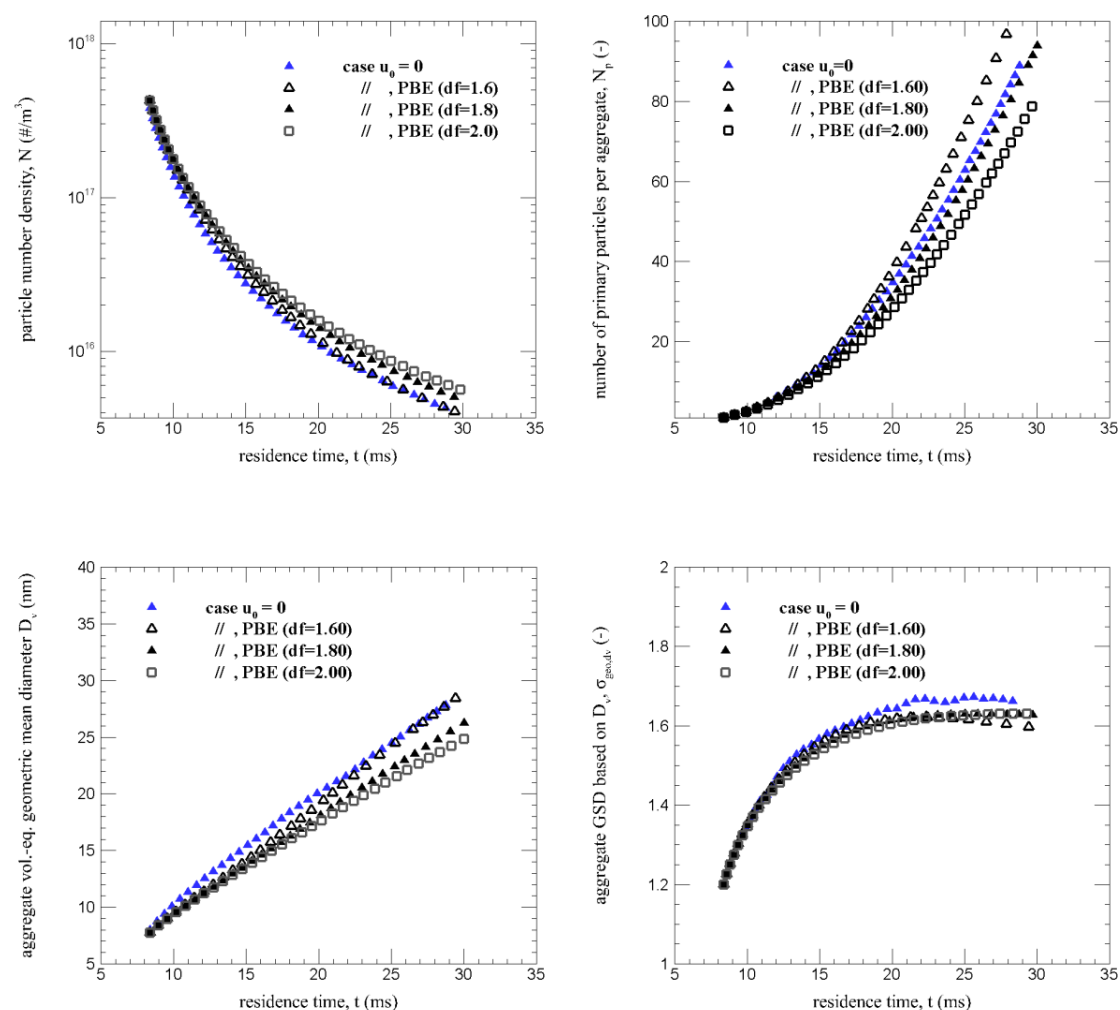
Fig. S1: Comparison between numerical simulation based on the Population Balance Equation (PBE) and MCAC. Three different fractal dimension are imposed for PBE simulations, namely $D_f = 1.6$, 1.8 and 2.0 with a constant prefactor $k_f = 1.40$.

References

Friedlander, S. K. (2000). Smoke, dust, and haze (Vol. 198). New York: Oxford University Press.

Prakash, A., Bapat, A. P., & Zachariah, M. R. (2003). A simple numerical algorithm and software for solution of nucleation, surface growth, and coagulation problems. *Aerosol Science & Technology*, 37(11), 892-898.

Thajudeen, T., Gopalakrishnan, R., & Hogan Jr, C. J. (2012). The collision rate of nonspherical particles and aggregates for all diffusive Knudsen numbers. *Aerosol Science and Technology*, 46(11), 1174-1186.

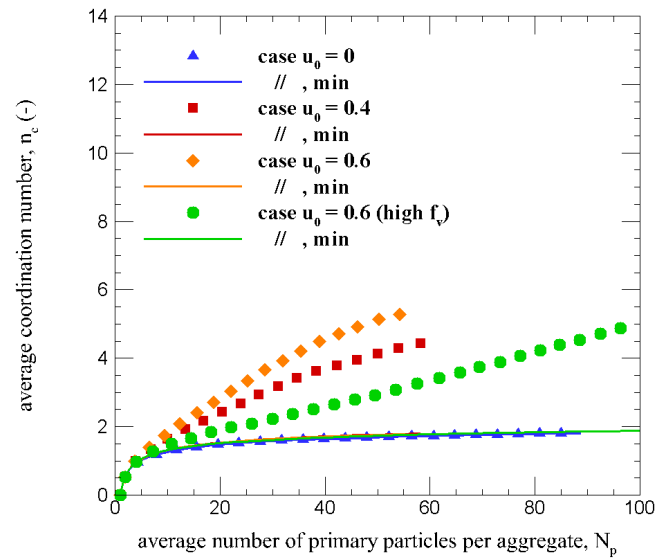# Coordination number and overlapping coefficient

Fig. S2: The average coordination number presented as a function of the average number of monomers per aggregate.
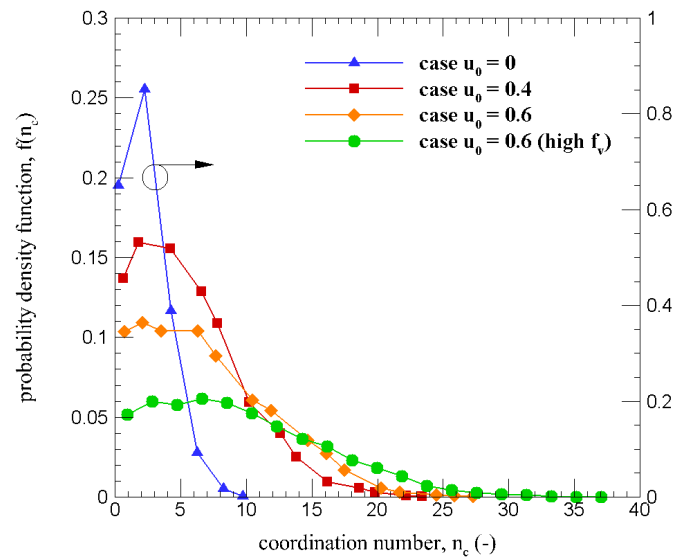

Fig. S3: Distribution of the local coordination number (for each monomer) at the end of the simulation (t = 30 ms). This is obtained when analyzing all the monomers belonging to the system.
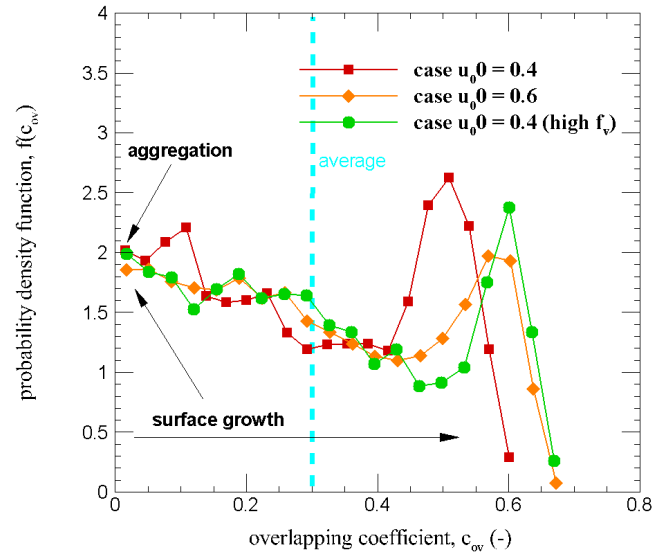
Fig. S4: Distribution of overlapping coefficients at the end of the simulation (t = 30 ms). This is obtained when analyzing all the pairs of monomers in contact belonging to all the aggregates in the system.

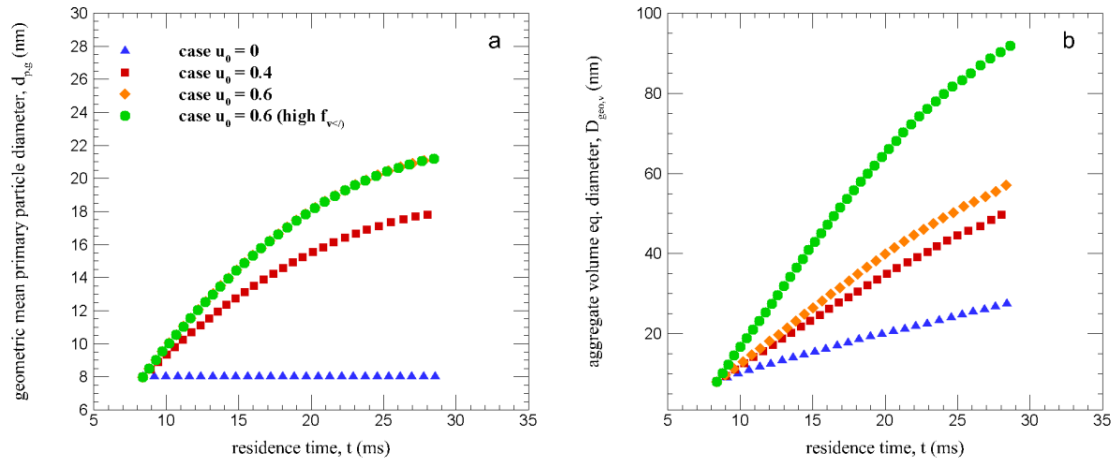## Primary particle and aggregate geometric mean diameters

Fig. S5: Primary particle (a) and aggregate (b) geometric mean volume-equivalent diameter as a function of time.

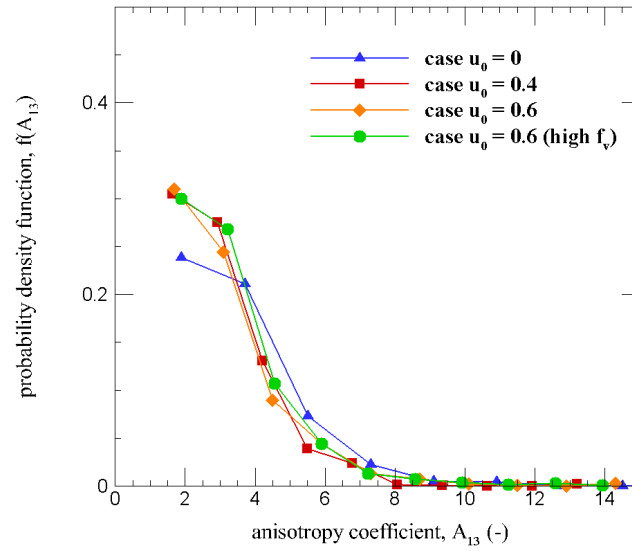# Distribution of the anisotropy coefficient

Fig. S6: Distribution of the anisotropy coefficient at the end of the simulation (t = 30 ms). The inertia moment matrix of the discretized aggregate is calculated, subsequently the anisotropy coefficient is determined as the ratio of the minimum and maximum eigenvalues of the inertia matrix.

Fitting the pair correlation function

As explained in the main manuscript, a direct fit of the pair correlation function ($A(r) = A_{pp} + A_{agg}$) searching the 6 parameters ($\varphi, D_f, \beta, \xi_{max}, \xi, \widetilde{r_{p,v}}$) is quite difficult. In this context, a fit-by-parts procedure is proposed as described as follows. The main idea of this procedure is to fix some parameters by fitting the numerically determined $A(r)$ by parts.

Step 1: select the part of the numerically determined $A(r)$ for $r < 5r_{p,v}$ where $r_{p,v}$ is the volume equivalent average primary particle radius. When fitting this part of the pair correlation function we have $A_{pp} \gg A_{agg}$ and therefore a reliable fit can be done to search $\widetilde{r_{p,v}}$. Once the parameter $\widetilde{r_{p,v}}$ has been found, it is kept constant for the following steps.

Step 2: select the part of the numerically determined $A(r)$ for $5r_{p,v} < r < 13r_{p,v}$. In this zone we have $A_{agg} \gg A_{pp}$. When the fractal zone is well stablished a reliable fractal dimension D_f can be obtained. Once again, upon finding D_f it is considered fixed for the following steps.

Step 3: Fix both $\widetilde{r_{p,v}}$ and D_f to the values found as described in steps 1 and 2, respectively. Conduct a new fit to find the remaining 4 parameters ($\varphi, \beta, \xi_{max}, \xi$).